Spins, charge radii and magnetic moments of neutron-rich Mn isotopes measured with bunched beam Collinear Laser Spectroscopy

Wouter GINS

Promotor: Prof. dr. Gerda Neyens
KU Leuven
Begeleider: Hanne Heylen
KU Leuven

Proefschrift ingediend tot het
behalen van de graad van
Master of Science in de Fysica

Academiejaar 2013-2014

It's gone, it's done.

—FRODO BAGGINS

Dankwoord

Deze thesis zou niet tot stand zijn gekomen zonder de hulp, begeleiding en aanmoediging van anderen. Bij deze wil ik deze mensen vermelden en bedanken voor hun bijdragen.

Allereerst zou ik prof. Gerda Neyens willen bedanken, zowel om mij een project te geven waar ik mij op kon uitleven, als om mij de vrijheid te geven om dit toch een beetje op mijn manier te doen. Zeer hartelijk bedankt!

Hanne, bedankt voor de (bijna) dagelijkse begeleiding en vergelijking van resultaten, en de sociale druk om toch niet al te veel pauze te nemen. Je bijna-typische "Goeie vraag, zoek maar eens op" antwoord op veel van mijn vragen, met een hint waar het verband mee houdt, heeft mij zeer veel doen bijleren.[†] Ook bedankt om mij een paar jaar geleden te overtuigen om kernfysica te doen met je enthousiasme, het blijft de beste academische beslissing die ik tot nog toe heb gemaakt!

I would also like to thank Bradley, whose analysis of the same data helped me convince myself I was on the right track, as well as explaining numerous things about the experiment. De rest van de Nuclear Moments Group wil ik ook bedanken voor de afleidingen die altijd zeer welkom waren! Ik wil ook even Jasna speciaal vermelden, zowel voor het klaarstaan voor vragen in het prille begin van het academiejaar als de aanmoedigingen de laatste paar weken/maanden. Ook de Wina-vriendjes die vaak nog uit het eerste jaar stammen mag ik niet vergeten, voor vijf fantastische studentenjaren.

Dan ben ik uiteindelijk bij mijn familie aanbeland. "Grote" broer, mijn interesse wekken in wetenschap is een van je betere beslissingen geweest. Burgie studeren daarentegen... Last but not least, Mama en Papa. Enorm bedankt om mij vijf jaar geleden te laten beginnen aan mijn studies, zonder enige verplichting buiten de begrijpelijke druk om te slagen.

—Wouter

[†]Ja, bij elke vraag die ik wil stellen vraag ik mij eerst af "is dit atomair, of nucleair?"

Abstract

In this work, the odd-even $^{51-63}_{25}$Mn isotopes have been analyzed using collinear laser spectroscopy, from which the magnetic dipole moment and the change in change in mean square charge radius can be determined. The magnetic moment is very sensitive to the composition of the total nuclear wave function, while the charge radius gives information about the relative size and degree of deformation of the nucleus. An additional advantage of collinear laser spectroscopy is the possibility of direct measurement of the nuclear spin.

The main motivation behind the study of these isotopes is to investigate the change in nuclear structure when approaching neutron number $N = 40$. This region is of interest due to the apparent doubly magic nature of $^{68}_{28}$Ni$_{40}$, which is not seen in the $N = 40$ isotopes of $_{26}$Fe and $_{24}$Cr. Mn, situated between these elements, offers another perspective due to its uncoupled proton.

Based on the observed spectra and extracted moments, spins were assigned to ^{59,61,63}Mn. The extracted magnetic moments indicate that there is a contribution to the total nuclear wave function of neutrons that are excited above $N = 40$. This means that $N = 40$ is not a shell closure anymore for Mn.

Samenvatting

In dit werk zijn de oneven-even $^{51\text{-}63}_{25}$Mn isotopen bestudeerd door gebruik te maken van collineaire laser spectroscopie, waarbij het magnetisch dipoolmoment en verandering in gemiddelde kwadratische ladingsstraal kunnen worden bepaald. Het magnetisch dipoolmoment is heel gevoelig voor de compositie van de volledige nucleaire golffunctie, en de ladingsstraal geeft informatie over de relatieve grootte en deformatie van de kerntoestanden. Een bijkomend voordeel van collineaire laser spectroscopie is de mogelijkheid van een rechtstreekse meting van de kernspin.

Het hoofddoel van deze studie is om de verandering in kernstructuur bij het naderen van $N = 40$ in kaart te brengen. Deze regio is interessant door de schijnbaar dubbel magische aard van $^{68}_{28}$Ni$_{40}$, welke niet gezien wordt in de $N = 40$ isotopen van $_{26}$Fe en $_{24}$Cr. Mn, gesitueerd tussen deze laatste twee elementen, biedt een ander perspectief in deze regio door zijn ongekoppeld proton.

Gebaseerd op de geobserveerde spectra en bekomen momenten zijn kernspins toegewezen aan ^{59,61,63}Mn. De bekomen magnetische momenten wijzen op een contributie tot de golffunctie van neutron excitaties boven $N = 40$. Dit houdt in dat $N = 40$ geen schillensluiting meer is voor Mn.

Vulgariserende Samenvatting

Het hoofddoel van veel kernfysisch onderzoek is het bestuderen hoe de atoomkern gestructureerd is, en waarom. Hierbij worden de eigenschappen van de sterke en zwakke kernkracht, actief in atoomkernen, in kaart gebracht. Theorie en experiment vullen elkaar hierbij aan: de eigenschappen van deze kernen worden vergeleken met modellen, en deze modellen kunnen op hun beurt verbeterd worden door de nieuwe experimentele resultaten te verwerken. Deze theorieën kunnen dan ook voorspellingen doen die experimenteel onderzocht kunnen worden.

De kernstructuur van stabiele isotopen is redelijk goed gekend, daar deze makkelijk te produceren en bestuderen zijn. De modellen die hierop gebaseerd zijn, worden getoetst door *exotische* kernen te bestuderen. Deze exotische kernen verschillen van gewone kernen door hun gebrek, of overvloed, aan neutronen ten opzichte van de stabiele isotopen, wat tot meer onderlinge interacties leidt. Deze kernen zijn nagenoeg altijd kortlevend, wat zowel de productie als bestudering ervan een grotere uitdaging maakt. Langs de andere kant worden nieuwe kernfysische fenomenen ontdekt in deze kernen, wat onze kennis van de kernkrachten uitbreidt. Onderzoek op deze exotische kernen is dus zeer interessant, zowel voor de technische uitdaging als de kennisuitbreiding.

In de kwantummechanische berekeningen van de kernstructuur komen ook "magische" getallen naar voor. Deze komen overeen met hoeveel protonen of neutronen samensmelten tot een extra stabiel systeem. Indien deze magische kernen tevens exotisch zijn, kan men veel leren over het verloop van de kernstructuur in functie van het aantal neutronen of protonen.

In deze thesis is het element mangaan onderzocht, wat 25 protonen heeft. Het aantal neutronen was telkens even, en varieerde van 26 tot 38 neutronen. Het doel was om het verloop naar 40 neutronen te bestuderen, want dit is in sommige modellen een magisch getal. De structuur van nikkel ligt in de lijn van deze modellen: bepaalde eigenschappen bevestigen inderdaad de $N = 40$ magiciteit. Voor andere eigenschappen is er echter geen extra stabiliteit te bespeuren, en voor ijzer en chroom, respectievelijk 26 en 24 protonen, is 40 op geen enkele wijze nog een magisch getal. Mangaan, dat met zijn oneven aantal protonen meer interacties kan aangaan, is daarom een uitstekende kandidaat om de regio verder te bestuderen.

Het experiment steunt op collineaire laser spectroscopie, waarbij de kernstructuur met een laser wordt afgetast. Sterk vereenvoudigd kijkt men naar het magnetisch karakter van de kern, wat heel gevoelig is voor de kwantummechanische samenstelling van de kern. De resultaten worden dan vergeleken met de voorspelling van een model dat voor deze regio in de kernkaart ontwikkeld is. Dit model neemt aan dat $N = 40$ een magisch aantal neutronen is. Als experiment en theorie niet overeenkomen, kan dat erop wijzen dat $N = 40$ niet magisch is.

Bij het vergelijken van de experimentele waarde en de theoretische voorspelling ziet men een afwijking van het model wanneer men dichter bij 40 neutronen komt. Hieruit besluiten we dat ook voor mangaan 40 neutronen geen magisch getal meer vormen.

Contents

List of Symbols

$\delta\nu$ Isotope shift

ℓ Angular momentum

$\hat{\mu}$ Magnetic dipole moment operator

$\hat{H}_{\text{res}}$ Residual part of the Hamiltonian

$\hat{H}_{\text{s.p.}}$ Single particle Hamiltonian

$\hat{Q}$ Electric quadrupole moment operator

$\hat{T}$ Kinetic energy operator

$\hat{V}_{ik}$ Potential energy operator between nucleons i and k

μ Magnetic dipole moment

ν Frequency

A Hyperfine parameter related to the magnetic dipole moment

B Hyperfine parameter related to the electric quadrupole moment

c Speed of light in vacuum

e Effective charge

e Elementary charge

F Field shift factor or coupling of spins I and J

I Nuclear spin

J Electronic spin

M Mass shift factor

m Mass of an atom

Q Electric quadrupole moment

U Potential energy.

V_{zz} Electric field gradient

List of Figures

List of Tables

Introduction

One region of the nuclear chart where current theories are extensively tested is the region around Ni. This work focused on neutron-rich, odd mass $_{25}$Mn isotopes. For several of the investigated isotopes, nuclear information such as spin and magnetic moment were not yet measured prior to a collinear laser spectroscopy experiment, carried out in November 2012.

This thesis will describe the experiment and the data analysis procedure, as well as an interpretation of the results. Before discussing this, an introduction is given to establish the conventions used in this work.

Chapter 1 introduces nuclear structure and hyperfine interactions. Chapter 2 gives an overview of collinear laser spectroscopy, introducing the background necessary for the discussion of the experiment and results.

Chapter 3 motivates the experiment, giving examples of already obtained nuclear structure information and trends in the neighborhood of manganese. Specifically, the evolution of magic numbers and relevant nuclear energy levels are discussed.

Chapter 4 describes the full experiment and the data analysis of the experiment. The results are discussed in Chapter 5. Chapter 6 concludes this thesis, briefly summarizing the results given in Chapter 5 and coupling back to the motivation in Chapter 3.

Part I

Theoretical preliminaries

Chapter 1

Nuclear structure

> There's so much that we share
> that it's time we're aware,
> It's a small world after all

<div align="right">

SHERMAN BROTHERS

</div>

A small introduction to nuclear structure will be given in this chapter, focusing on aspects that are of particular importance for this thesis. This includes a general introduction to the shell model, the Nilsson deformed model, and nuclear moments. The hyperfine interaction, the interaction between the nucleus and electronic magnetic and electric fields in the atom, is also discussed.

1.1 Nuclear shell model

The nucleus is an example of a quantum many-body system. Solving the equations of motion for this system presents a problem akin to the classical many-body problem in that it is analytically unsolvable. In this case, the Hamiltonian that has to be considered is [1]

$$\hat{H} = \sum_i \hat{T}_i + \frac{1}{2} \sum_{i \neq k} \hat{V}_{ik} (\vec{r}_i - \vec{r}_k). \tag{1.1}$$

In the shell model approach, single particle solutions become available by introducing an average potential that is both felt and generated by each nucleon:

$$\hat{H} = \underbrace{\sum_i \hat{T}_i + \sum_i \hat{U}_i (\vec{r}_i)}_{\hat{H}_{\text{s.p.}}} \underbrace{- \sum_i \hat{U}_i (\vec{r}_i) + \frac{1}{2} \sum_{i \neq k} V_{ik} (\vec{r}_i - \vec{r}_k)}_{\hat{H}_{\text{res}}}, \tag{1.2}$$
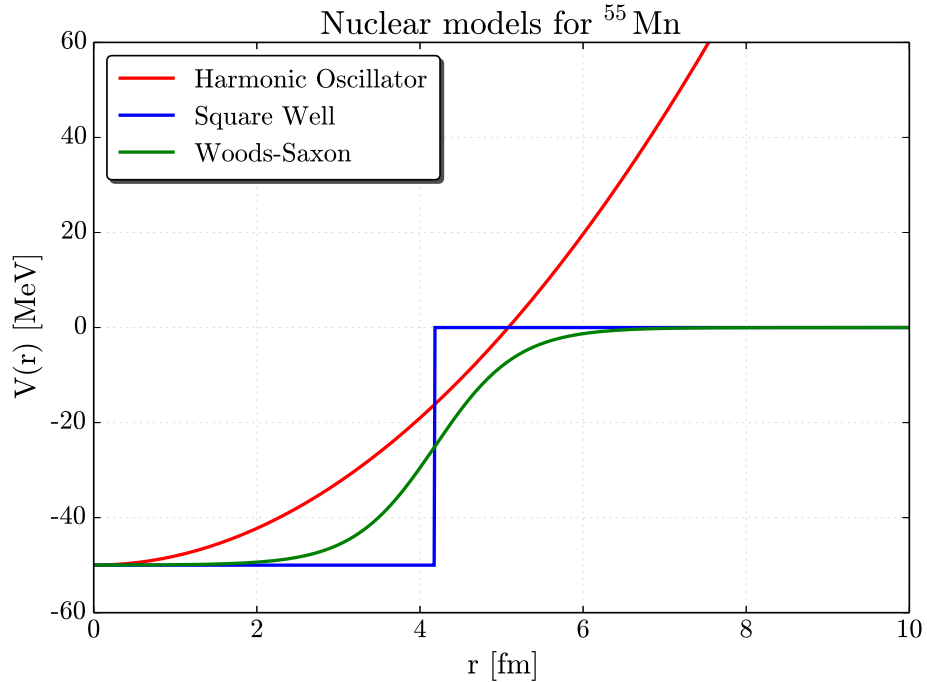
Figure 1.1: *As an example, the three different models are drawn for ^{55}Mn. As explained in the text, the harmonic oscillator suffers from a lack of a surface, while the square well is too sharp.*

where the residual part of the Hamiltonian is kept small, such that perturbation theory can be applied. The huge advantage of this form is that this can be solved using analytical or manageable numerical tools, since the single particle Hamiltonian ($\hat{H}_{\text{s.p.}}$) can be solved for each individual nucleon. The solutions obtained from this Hamiltonian provides the unperturbed single particle wave functions and energies. The full solution is then found using perturbation theory, in a well-defined valence space, to determine the eigenvalues of the total Hamiltonian. This is done for an effective interaction that is described by two-body matrix elements and some monopole corrections to the unperturbed single particle energies. There are different ways of modeling this average potential, each with their own (dis)advantages.

- The harmonic oscillator (HO) potential is an adequate approximation of the mean field potential generated by the nucleons, but suffers from an infinite separation energy, and lack of what can be considered a surface, which means that the potential generates a finite depth.

- The square well potential has a well defined surface, but is much too sharp. A more gradual increase in potential energy as a function of r is expected.

- The golden mean is a function that lies between these models, and is known as the Woods-Saxon potential, or Fermi function: [2]

$$U(r) = \frac{-V_0}{1 + \exp\left[\frac{(r-R)}{a}\right]}.$$ (1.3)

The parameters in this model can be assigned physical interpretations: V_0 is the depth of the potential well, typically $50\,\text{MeV}$, a is the skin thickness with a value of roughly $0.5\,\text{fm}$, and R is the mean radius of the nucleus, with an estimate given by $1.25A^{1/3}\,\text{fm}$, with A being the mass number. In Figure 1.1, the three models are illustrated in the case of ^{55}Mn. One possible derivation starts from the HO-model and improves it. This is done by adding a spin-orbit term and an angular momentum dependency. More information can be found in Ref. [3, 4].

In the following sections, the term 'valence space' will often be used. This valence space is the collection of single particle levels that are used as a basis in shell model calculations.

1.1.1 Shells and shell gaps

Solving the Schrödinger equation for the single particle Hamiltonian leads to discrete energy levels. Particularly large energy gaps allow us to group levels together in shells. The amount of nucleons needed to fill the subsequent shells are called magic numbers [2]. These magic numbers indicate a sizable energy difference between subsequent energy levels, leading to discontinuities in certain parameters such as separation energy. These were experimentally observed and serve as proof to the existence of magic numbers. Note that instead of the term magic number, shell closure is also used.

If these shell gaps are studied, they can be classified into two different classes: [5]

Harmonic Oscillator gaps: Shell gaps originating from the harmonic oscillator potential lead to different parities of the levels on either side of the gap. Since quadrupole excitations, characterized by $\Delta\ell = 2$, preserve parity, quadrupole excitations across a harmonic oscillator shell gap can only occur if two particles are excited at the same time.

Spin-Orbit gaps (SO): Spin-orbit interactions splits a quantum level with well-defined orbital momentum ℓ in two levels due to the interaction of the orbital
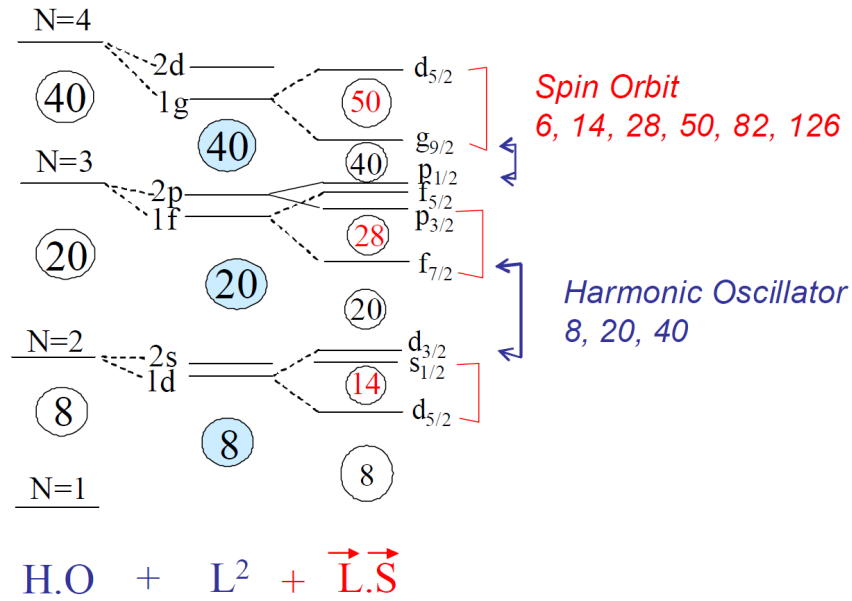
Figure 1.2: *The levels up to the $2d_{5/2}$-level, also presenting the evolution of the shell gaps as more terms are added to the harmonic approximation. Figure from Ref. [5].*

and spin angular momenta. The positive coupling $(\ell + s)$ lowers the energy, while the negative coupling $(\ell - s)$ gains in energy. This effect can lead to shell gaps between levels with the same parity and a difference of angular momentum ℓ of 2 on the sides of the gap. Here, quadrupole excitation is already possible at the 1p1h-level.

Figure 1.2 gives the lowest levels of the potential and the effect of different terms of the shell gaps, also indicating the class of the gap.

Up to now, the discussion focused on the single particle nature of the energy levels as determined by the average potential. Changes to these unperturbed single particle energies, and even their ordering, will occur due to the residual interaction between the nucleons. The monopole part of the residual two-body interaction will lead to a change in the single particle energy when the occupation of certain single particle levels is modified [1]. This monopole interaction leads to an evolution of the energy levels that depends on on the number of protons and neutrons in the nucleus.

The quadrupole correlation energy is the energy the system gains when it adopts a deformed shape or in a shell model context, when a shell is not completely filled. Indeed, correlations are not possible when a level is completely occupied by particles (or holes), and they are maximized when the level is half-full[†] [5]. Which

---

[†]Or half-empty, depending on your philosophical outlook.

configurations give rise to the highest correlation energy will depend on the nucleus, or more accurately, on which are the active valence proton and neutron levels. This correlation energy can lead to a shift in energy for some single particle levels, possibly creating or destroying shell gaps.

1.1.2 Configuration mixing

Up to now, the intuitive picture was that of nucleons moving in certain levels, and mainly staying there. This idea is viable, but calculations based on this assumption are only valid at closed shells. In isotopes with the highest occupied level in the middle of a shell, calculations based on the extreme single particle model break down [6].

To create better agreement between theory and experiment, the concept of configuration mixing is introduced. In a valence space where more than one single particle level is considered, different configurations can lead to the same observed spin [1]. Thus, instead of a single state, the wave function is a combination of states with mixing amplitudes α_i: [7]

$$|\Psi\rangle = |\phi_1\rangle \xrightarrow{\text{configuration mixing}} |\Psi\rangle = \sum_{i=1}^{N} \alpha_i |\phi_i\rangle. \tag{1.4}$$

Here, $|\Psi\rangle$ is the full nuclear wave function, $|\phi_i\rangle$ the wave function associated with state i, N the amount of configurations possible, and the mixing amplitude α_i. This mixing amplitude is related to the percentual contribution of that configuration to the full wave function.

1.2 Nilsson model

In the previous section, all theories were based on a spherical mean field potential, with possible deformation due to quadrupole correlations. Another approach can be used in which the single-particle basis is calculated from a quadrupole deformed potential, with the deformation represented by a parameter β_2 or ε. This single particle basis replaces the basis used in the simple shell model, so the need for additional interactions should be less.
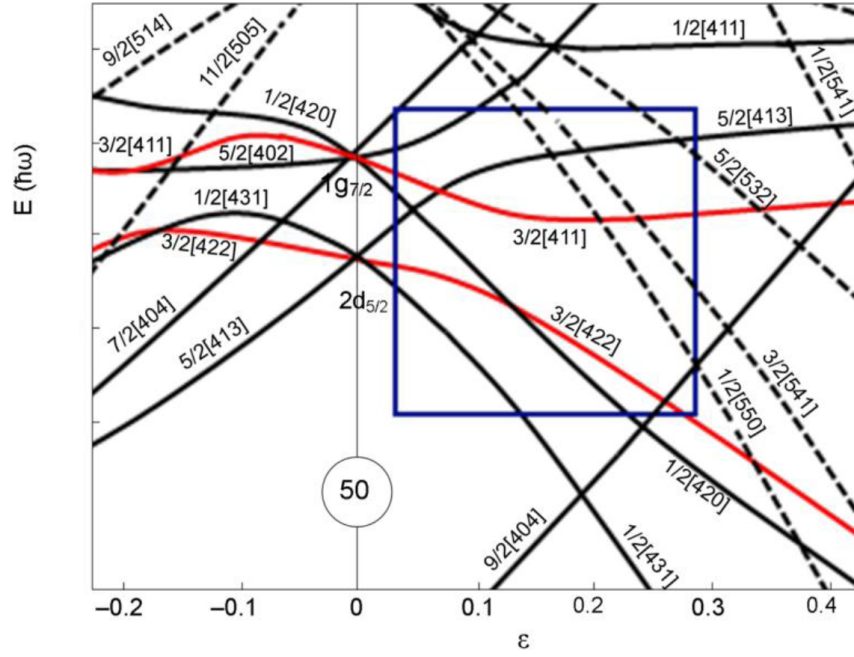
Figure 1.3: *An example of the energy levels in the Nilsson model. The repulsive effect of the two levels with the same K can be clearly seen. Figure taken from Ref. [3]*

In the Nilsson model approach, the harmonic oscillator term is modified by assuming an asymmetric oscillator, with the z-axis being the presumed symmetry axis: [3]

$$\hat{H}_{HO} \sim \omega_\perp^2 \left(x^2 + y^2 \right) + \omega_z^2 z^2. \tag{1.5}$$

Carrying out the calculations allows the expression of the energy levels in function of the previously introduced deformation parameters. The relation between these parameters[‡] is [8]

$$\varepsilon = 3 \frac{\omega_\perp - \omega_z}{2\omega_\perp + \omega_z}, \tag{1.6}$$

$$\beta_2 = \varepsilon \sqrt{\frac{16\pi}{45}}. \tag{1.7}$$

The most important feature from these relations is that the parameters have the same sign. Thus, a diagram as a function of one parameter can be interpreted in the same fashion as the other parameter.

One aspect of the Nilsson model is that the single particle level angular momentum I is no longer a good quantum number. The quantum number K, the projection of

---

[‡]Depending on the used convention, the symbol δ is used instead of ε, but it is the same parameter.

the angular momentum I on the symmetry axis, is the only good quantum number. Three other numbers are used to denote the level: $[Nn_z\lambda]$, with N the number of harmonic oscillator quanta, n_z the number of nodes in the wave function and λ the projection of the angular momentum on the symmetry axis. These numbers become good quantum numbers at large deformation, and are therefore called asymptotic quantum numbers. Due to the symmetry of the quantum number K, all Nilsson levels are twofold degenerate.

Another effect has to be taken into account in these diagrams: level-level repulsion. Energy levels with the same quantum numbers cannot cross, which is a general rule in quantum mechanics. Since K is the only good quantum number remaining, levels with the same K and parity will repel each other, as seen in Figure 1.3. The wave functions of these levels are highly mixed in the region where they repel each other.

1.3   Large scale shell model calculations

Shell model calculations start from the Hamiltonian in Eq. (1.1) and try to predict the properties of different nuclei. This is done by looking at the lowest energy eigenstates of the Hamiltonian for a certain spin I, from which nuclear observables can be derived. In order to do these calculations, a form for the residual interaction has to be proposed.

The process for such a calculation is, in general, divided in four steps [1]: the valence space and nucleons are specified, the configurations that span each J^π are determined, the Hamiltonian is evaluated in each span, and each Hamiltonian matrix is diagonalized. Different techniques exist to determine the span for each J^π and to effectively diagonalize the matrices. These techniques are needed, since the dimensionality of the generated matrices is very high. In the pf shell, dimensions lie between 10^6 and 10^9 [9].

It is important to note that these large scale shell model calculations are very different from the Nilsson model. Where the Nilsson model modifies the single particle energy levels, and is presented as a unified model, shell model calculations include the effect of deformation through collective behavior via the residual nucleon-nucleon interactions [10]. This is signified by non-zero off-diagonal matrix elements in the Hamiltonian. More specifically, an underlying SU(3) symmetry is important for quadrupole collectivity to emerge. For this symmetry to emerge, the correct orbits have to be included in the valence space [11].
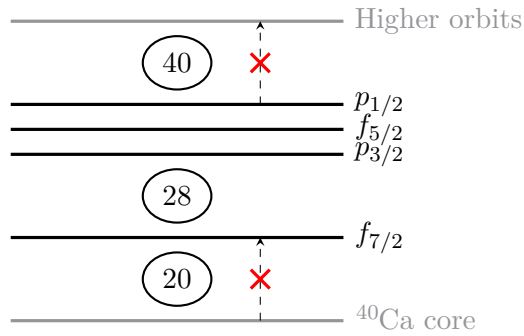
Figure 1.4: *The GXPF1 model assumes an inert ^{40}Ca core (gray), from which no excitations can occur. The active valence space is the full pf-shell (black), and excitations to higher lying orbits (gray) are not permitted. These levels and classification are used for both protons and neutrons.*

Different shell model codes use different methods for the span determination and diagonalization, while different interactions define different valence spaces and affect the evaluation of the Hamiltonian. In this work, the results are compared to ANTOINE shell model calculations, which uses the M-scheme to determine the span, and uses Lanczos diagonalization of the Hamiltonian. The interaction used in this work is the GXPF1 interaction [12], which assumes an inert $^{40}_{20}\text{Ca}_{20}$ core, a valence space formed by the pf shell and no interaction with higher lying orbits. This model is schematically illustrated in Figure 1.4.

1.4 Nuclear moments

A general introduction to nuclear moments is given first. Then, the magnetic dipole and electric quadrupole moment are treated. At the end of this section, the shell model predictions of the nuclear moments are introduced.

For more specialized treatment, the reader is referred to Refs. [1,2] for the general introduction, Ref. [1] for the magnetic and quadrupole moments and Ref. [6] for the moments in the shell model and configuration mixing corrections.

1.4.1 General introduction

The shape of the nucleus can only be effectively probed by the, relatively weak, electromagnetic interaction. If the stronger forces would be used, they would deform

the nucleus, thus removing any usable information. Therefore, the nucleus will be seen as a distribution of electric charges and currents, giving rise to different spatial configurations and thus different multipole configurations.

Considering that angular momentum is a good quantum number, the Wigner-Eckart theorem can be used to write diagonal matrix elements as [13]

$$\left\langle I, m_z \middle| \hat{T}_q^{(k)} \middle| I, m_z \right\rangle = (-1)^{I-m} \begin{pmatrix} I & k & I \\ -m & q & m \end{pmatrix} \left\langle I \middle\| \hat{T}^{(k)} \middle\| I \right\rangle , \qquad (1.8)$$

with T a tensor operator (which can be either Q for the electric moment or M for the magnetic moment operator). Due to parity considerations, the reduced matrix element, and therefore the full matrix element, is zero if the parity of the operator is negative. It can also be proven that the parity of the multipole moments is given by [1]:

$$\Pi \left(\hat{Q}^k \right) = (-1)^k , \qquad (1.9)$$

$$\Pi \left(\hat{M}^k \right) = (-1)^{k-1} , \qquad (1.10)$$

with $\hat{Q}^k$ and $\hat{M}^k$ respectively the electric and magnetic tensor operators of rank k. This means that only even electric and odd magnetic moments have a non-zero matrix element. Furthermore, the Wigner 3j-symbol in Eq. (1.8) imposes upper limits on the multipole order k that a nucleus possesses, based on the spin I. More specifically, the restrictions that the lower row must sum to zero and the upper row obeys the triangle inequality correspond to $q = 0$ and $k \leq 2I$.

Theoretically, all moments up to the limit imposed by the nuclear spin can be considered, but it is only in very rare cases that a moment with a rank higher than 2 makes a measurable contribution. Therefore, only the first order (dipole) moment and second order (quadrupole) moment will be discussed.

1.4.2 Magnetic dipole moment

The magnetic dipole operator $\hat{\mu}$ is a spherical tensor of rank $k = 1$. based on this fact, the projection theorem allows the writing in a simple form. This theorem is actually a restatement of the Wigner-Eckart theorem [14]:

$$\left\langle \alpha', jm' \middle| V_q \middle| \alpha, jm \right\rangle = \frac{\left\langle \alpha', jm \middle| \vec{J} \cdot \vec{V} \middle| \alpha, jm \right\rangle}{\hbar^2 j (j+1)} \left\langle jm' \middle| J_q \middle| jm \right\rangle , \qquad (1.11)$$

with $\vec{V}$ a vector operator. This equation states that the matrix element of any vector operator is proportional to the matrix element of the total angular momentum operator [13, 14]. This justifies the writing of the operator as proportional to the total angular momentum, with the introduction of g-factors [13]:

$$\hat{\mu} = \frac{\mu_N}{\hbar} g \vec{I}, \qquad (1.12)$$

with μ_N the standard nuclear magneton. A more intuitive approach can also be used, based on classical electrodynamics such as developed in Ref. [15]. There, the magnetic moment is shown to be proportional to the angular momentum of a rotating object, leading to a similar formula as in the quantum mechanical case.

The moment itself is defined as the expectation value of z-component of this operator at maximal projection, due to the $q = 0$ restriction [2, 16]:

$$\mu = \langle I, m = I | \hat{\mu}_z | I, m = I \rangle = g \mu_N I. \qquad (1.13)$$

This can be split into an orbital and intrinsic (spin) angular momentum part, resulting in the g_ℓ and g_s-factors. As the orbital g-factors are due to the orbiting charge of the nucleon, g_ℓ is 1 for protons and 0 for neutrons.

The g_s-factor for the proton would be, based on the Dirac theory of spin-$1/2$ particles, exactly 2. The neutron, due to being uncharged, would have a g_s-factor of 0. However, measurements have revealed that, for free nucleons, the value is [17]

$$\text{protons}: \quad g_s = 5.585694713 \pm 0.000000046,$$
$$\text{neutrons}: \quad g_s = -3.82608545 \pm 0.00000090.$$

This deviation from the expectation points to the underlying internal structure of the nucleons, which is evidence that they cannot be considered elementary point particles. Quantum field theories considering the quark structure accurately reproduce these magnetic moments.

1.4.3 Electric quadrupole moment

Regarding the electric quadrupole moment, one cannot make the simplification with the projection theorem like in the case of the magnetic dipole moment. The general

$Q > 0$ $Q = 0$ $Q < 0$
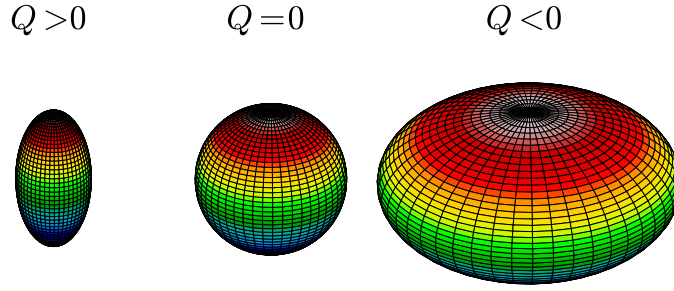
Figure 1.5: *From left to right: a prolate shape for $Q > 0$; a normal sphere for $Q = 0$; an oblate shape for $Q < 0$.*

form in the multipole expansion must thus be used, yielding as operator [1]

$$\hat{Q}_q^{(2)} = \sqrt{\frac{16\pi}{5}} \sum_i^A e_i r_i^2 \hat{Y}_{q,i}^{(2)}, \tag{1.14}$$

with the index i running over each nucleon and $\hat{Y}^{(2)}$ the second spherical harmonical operator. The spectroscopic quadrupole moment Q_s is defined as being the result of the $q = 0$ component for the maximal projection. Using the Wigner-Eckart theorem, one finds a guaranteed result of 0 for the spectroscopic moment for both $I = 0$ and $I = 1/2$. This means the spectroscopic moment is zero, but this does not necessarily mean that the nucleus doesn't have an intrinsic electric quadrupole moment.

The physical interpretation of the intrinsic quadrupole moment is the nucleus' deviation from spherical symmetry. The sign of the intrinsic quadrupole moment leads to different forms of this deviation (see Figure 1.5). The possible deformations from a sphere are a prolate and an oblate shape. Respectively, this corresponds to being stretched in the z direction ($Q > 0$) and stretched in the x and y direction ($Q < 0$). The relation between the observed spectroscopic quadrupole moment and the intrinsic quadrupole moment is model dependent. The nuclear deformation is thus a model-dependent observable, while the spectroscopic quadrupole moment is not.

1.4.4   Moments in the shell model

Effective single particle model

In the effective single particle model, the physical quantities of a nucleus are determined by the last unpaired valence nucleon. The other valence nucleons are assumed to couple together to form spin 0 and do not contribute to the moments.

Using the shell model as a starting point, and following the effective single particle model, one can find expressions for the nuclear multipole moments. Considering the assumptions involved, this approach is expected to be successful very near doubly magic nuclei only.

For the magnetic dipole moment, an expression for so-called Schmidt moments can be derived. These are [2]

$$\left(j = \ell + \frac{1}{2}\right) \rightarrow \quad \mu = \left[g_\ell\left(j - \frac{1}{2}\right) + \frac{1}{2}g_s\right]\mu_N, \tag{1.15}$$

$$\left(j = \ell - \frac{1}{2}\right) \rightarrow \quad \mu = \left[g_\ell\frac{j\left(j + \frac{3}{2}\right)}{j + 1} - \frac{1}{2}\frac{1}{j + 1}g_s\right]\mu_N. \tag{1.16}$$

Filling in the values for either the proton or the neutron in an orbit with angular momentum j leads to an estimation of the magnetic moment for an unpaired nucleon in that orbit.

When reviewing the data on magnetic moments (see Figure 1.6a), the general trend as shown by the Schmidt lines is present; however, the experimental values are scattered rather wildly throughout the region defined by the two lines. A better approximation can be made by adjusting the values of the g-factors, with the argument that the values for the free nucleons are damped through the difference in the surrounding meson cloud inside a nucleus. There is still significant scatter around the best fitting line; this means that there is another mechanism at work, which is not explained by the single particle (unperturbed) shell model.

In a derivation analogous to the Schmidt moments, the quadrupole moment in the extreme single particle model is given by [2]

$$Q_s = -e\frac{2\ell - 1}{2\left(\ell + 1\right)}\left\langle r_j^2 \right\rangle \tag{1.17}$$
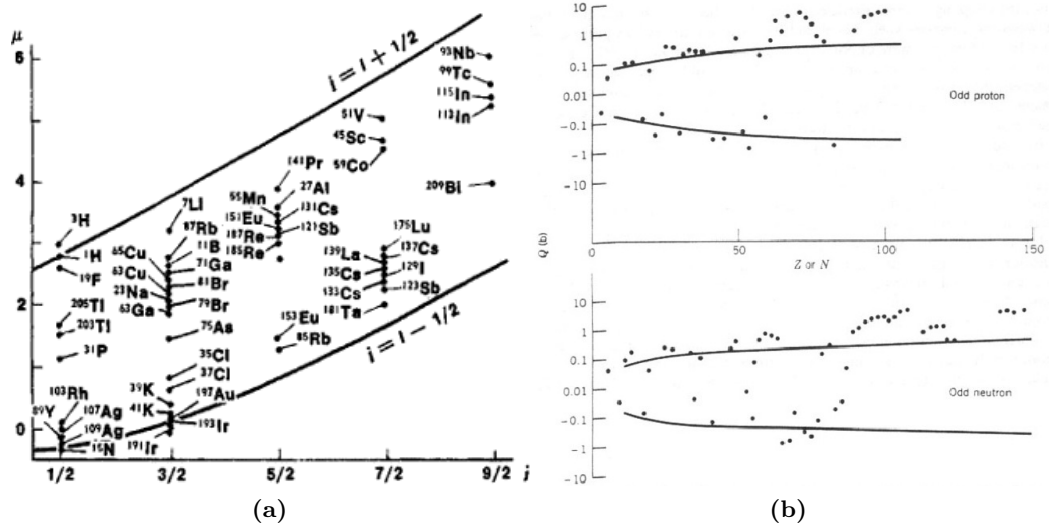
Figure 1.6: (a) *Using the expressions* (1.15) *and* (1.16)*, the solid lines represent the two possible values predicted for the odd-proton case.* (b) *For both the odd-proton and odd-neutron case, a non-zero value is measured for the quadrupole moment. The solid line indicate the limits predicted by shell model considerations, which agrees with the data except in certain regions. Figures taken from Refs. [2, 18].*

with $e = 1$ for protons, and a single particle quadrupole moment of zero for the odd-neutron case. Comparing the predicted values with the experimental ones, the only quantity that is predicted correctly is the sign of the moment. However, the values are consistently underestimated, indicating a lack of accuracy in the model. Furthermore, this is only the case for an odd proton number. The situation for an odd neutron number is even worse, with definite non-zero values being measured. The data, and the $\langle r^2 \rangle$ dependency, can be found in Figure 1.6b.

This prediction can be improved by introducing an effective charge [1]. This effective charge can be linked with the polarization induced in the nucleus, which is the mechanism through which neutrons, although electrically neutral, can still contribute to the quadrupole moment due to the proton-neutron interaction.

Configuration mixing correction

As explained in the previous section, the shell model can be extended by including configuration mixing due to the residual nucleon-nucleon interaction, which creates deviations from the expectation values of operators proportional to the mixing amplitudes. Using perturbation theory, and considering only two-body residual

interactions, four different types of configuration mixing can be formulated [6]. However, all these types depend on the valence space under consideration. Extending the valence space generally improves the accuracy of the predictions, but this approach comes with a high computational price. The dimensionality of the problem skyrockets, which means that theorists have to come up with an efficient way of simplifying the problem. Limiting the valence space to the known important levels also helps in keeping the computational difficulty under control.

As an example, consider a nucleus where both the protons and the neutrons completely fill the shell model levels, both up to some shell gap. Then, if the valence space is restricted to the completely filled levels, no mixing occurs. Extending the valence space allows for configuration mixing. Certain assumptions, such as the nature of the residual interaction, restrict the possible configurations. Different types of mixing are thus possible, and depend on the assumptions about the residual interaction [6].

The main result is the adjustment of matrix elements. In a situation where the mixing amplitudes are so small that the squared amplitudes can be neglected, the expectation value of a Hermitian operator F is [6]

$$\langle F \rangle \approx \langle \phi_1 | F | \phi_1 \rangle + 2 \sum_{i \neq 1} \langle \phi_1 | F | \phi_i \rangle , \qquad (1.18)$$

where selection rules can be introduced to more easily evaluate the mixing matrix element. If the case of the magnetic moment is taken, the principal quantum numbers and the orbital angular momenta have to be equal for a non-vanishing off-diagonal matrix element. After calculations, it follows that configuration mixing between levels of $j_1 = \ell_1 + 1/2$ and $j_2 = \ell_1 - 1/2$ has the greatest effect on the magnetic moment. Putting these calculations to use, a much better agreement is found between the theoretical values of the magnetic moment and the experimental data. For the results and comparison of these calculations, see Ref. [6].

Investigating this effect for the quadrupole moment, configuration mixing agrees fairly well with the observed values, especially in the medium-weight area of the nuclear chart [6]. However, one has to keep in mind that most measurement techniques do not measure the quadrupole moment directly. They are sensitive to the product QV_{zz}, with V_{zz} the electric field gradient (EFG) at the site of the implanted nucleus. The fact that this gradient has to be derived often from theoretical models which nowadays can reach a precision of up to 10%, leads to much less accurate measurements.

1.5 Hyperfine structure

When the different energy levels for an atom are calculated or probed, the interaction between the electronic and nuclear spin has to be considered, giving rise to splittings of atomic levels and shifts. The interaction between these two spins is called the hyperfine interaction. The adjustments to the atomic energy levels due to these hyperfine interactions are of the order of μeV, much smaller than the lower order correction called the fine structure. The first order approximation of this hyperfine interaction gives rise to a monopole shift, while higher order (mainly dipole and quadrupole) corrections induce the splitting of the electronic fine structure levels with spin J into hyperfine levels characterized by a total spin F [16].

Through the hyperfine interaction the nuclear spin I and electronic spin J are coupled together to another quantum number F, with the relative orientation of the spins determining the value of F. The value of F lies within the range

$$F \in \{|I - J|, |I - J| + 1, \ldots, I + J\}. \tag{1.19}$$

In this coupling, rotational invariance for the electronic spin is assumed. As soon as an external magnetic field is applied, a preferential axis is chosen and the coupling to F is no longer valid, since the electronic spin (which couples 2000 times more strongly to the magnetic field than the nuclear spin) no longer possesses spherical symmetry [2,16]. This means that two distinct situations arise in the consideration of hyperfine interactions: the effect in free atoms, and the effect on atoms implanted in solids. Since the experimental technique used in this work is based on the interaction in free atoms, only this situation is explored. For the hyperfine interaction based on atoms in solids, see Ref. [16].

1.5.1 Dipole interaction

For a magnetic dipole interaction, the Hamiltonian is given by the expected equation

$$\hat{H} = -\hat{\mu} \cdot \hat{B}, \tag{1.20}$$

which is akin to the classical interaction of a current with an external magnetic field. As shown before, the magnetic moment operator is proportional to the nuclear spin. The magnetic field in the expression above is the magnetic field as felt by the nucleus. This field is generated by the atomic electron cloud. A semi-classical reasoning then

states that the generated field is proportional to the electronic spin. Rewriting this in observables, the expression for the magnetic hyperfine interaction is

$$\hat{H} = -\frac{\mu B}{\hbar^2 IJ} \hat{I} \cdot \hat{J} = -\frac{\mu B}{2\hbar^2 IJ} \left(\hat{F}^2 - \hat{I}^2 - \hat{J}^2 \right). \tag{1.21}$$

Evaluating the matrix element of this Hamiltonian for a certain F state, the energy shift of that particular F state with respect to the electronic fine structure level with spin J is given by [16]

$$\Delta E = \left\langle F \middle| \hat{H} \middle| F \right\rangle = -\frac{1}{2} AC, \tag{1.22}$$

with

$$A = \frac{\mu B_J}{IJ}, \tag{1.23}$$

$$C = F(F+1) - I(I+1) - J(J+1). \tag{1.24}$$

This hyperfine A-parameter gives the energy scale of the splitting, and is what is used to determine the magnetic moment, and g-factor, of isotopes.

1.5.2 Quadrupole interaction

The Hamiltonian of the quadrupole interaction due to the charge-charge interaction between the atomic and nuclear charges is [16]

$$\hat{H}_{qq} = -\frac{e^2 NZ}{5\epsilon_0} \left(\frac{1}{r_e^3} Y^2 (\theta_e, \phi_e) \right) \cdot \left(r_n^2 Y^2 (\theta_n, \phi_n) \right), \tag{1.25}$$

with N number of electrons and Z the number of protons in the considered atom. The subscript e refers to the electronic component, and n to the nuclear. A calculation can again be performed to deduce the energy splitting from this expression. The final result is [2]

$$\Delta E = -B \frac{\frac{3}{4} C(C+1) - I(I+1)J(J+1)}{2I(2I-1)J(2J-1)}, \tag{1.26}$$

with

$$B = eQ_s V_{zz}, \tag{1.27}$$

and C as before. In the expression for B, e is the elementary charge, Q_s is the spectroscopic quadrupole moment and V_{zz} is the electric field gradient at the core of the nucleus.

Note that this expression again forbids a spin of $1/2$ or 0, since the denominator would be 0 in that case, making the expression undefined.

1.5.3 Combined interactions

The combined interaction leads to a shift of the atomic fine structure energies given by

$$\Delta E_{tot}\left(A,B,F,I,J\right) = -\frac{1}{2}AC - B\frac{\frac{3}{4}C\left(C+1\right) - I\left(I+1\right)J\left(J+1\right)}{2I\left(2I-1\right)J\left(2J-1\right)}. \tag{1.28}$$

The total shift induced by these interactions is also called the hyperfine splitting.

When considering the transition frequency between atomic levels, this frequency is modified by the lower and upper hyperfine splitting, such that the deviation of the transition frequency from the unperturbed fine structure frequency is given by:

$$\Delta\nu = -\Delta E\left(A_{low}, B_{low}, F_{low}, I, J_{low}\right) + \Delta E\left(A_{up}, B_{up}, F_{up}, I, J_{up}\right) + \text{CoG}, \tag{1.29}$$

with ΔE as in Eq. (1.28). The additional parameter is the central frequency or center of gravity (CoG) of the hyperfine spectrum, and it is related to the fitted fine structure transition frequency. From this parameter, an isotope dependent shift called the isotope shift is calculated. Figure 1.7 gives an illustration of this effect.

Although the absolute intensity of a transition depends on different factors, among which the number of excited ions/atoms and the detection efficiency, the relative intensity of each of the transitions can be calculated[§]. For different derivations, the reader is referred to Refs. [19, 20] and the references therein. Independent of the approach, the final result of the calculation is that

$$\mathcal{I}\left(i,f\right) \propto \left(2F_i + 1\right)\left(2F_f + 1\right)\begin{Bmatrix} J_f & F_f & I \\ F_i & J_i & 1 \end{Bmatrix}^2. \tag{1.30}$$

In the course of this calculation, certain selection rules appear for the hyperfine transitions due to electric dipole radiation. These are

$$\Delta J = 0, \pm 1 \quad \wedge \quad J_f + J_i \neq 0, \tag{1.31}$$

$$\Delta F = 0, \pm 1 \quad \wedge \quad F_f + F_i \neq 0. \tag{1.32}$$

[§]Notice the absence of the word *easily*.
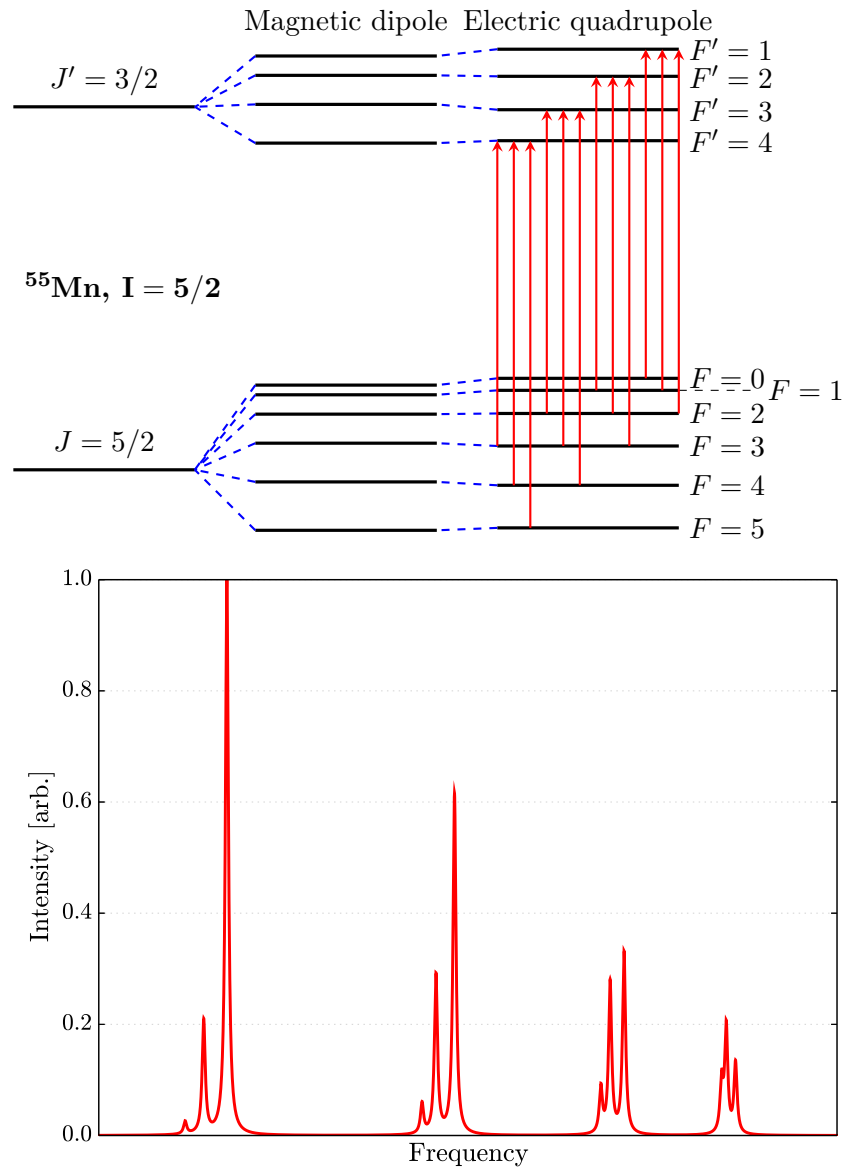
Figure 1.7: *The hyperfine splitting of ^{55}Mn as depicted above gives rise to a spectrum such as in the lower plot. The hyperfine A and B parameters as obtained from the experiment have been used for the simulation. This simulated spectrum has a linewidth of 57 MHz, which is the calculated natural linewidth of the energy level. The peaks, as seen from left to right, correspond to the transitions in the diagrams, drawn from left to right. The peak intensity is normalized to the strongest transition, with the relative intensities given by the Racah formula (1.30). For the diagram, the presented splitting due to the dipole and quadrupole interaction is to scale within each level, since the quadrupole splitting is orders of magnitude smaller than the magnetic splitting.*

Eq. (1.30) gives transition intensities, or rather relative intensities, that are known as Racah intensities. Using these theoretical intensities allows to set up a fitting routine using Eq. (1.29) to fit the relative peak positions and Eq. (1.30) to calculate the relative peak intensities. This leaves one parameter for the amplitudes and only the central frequency and the A and B factors as free parameters to determine the relative positions.

The relative peak intensities are sensitive to the assumed nuclear spin, and can thus often be used to determine the nuclear spin. The fitted amplitudes are compared to the Racah intensities. Spin values for which the relative intensities are comparable can not be excluded by this method however.

1.5.4   Isotope shift

If the central transition frequency in a series of isotopes is investigated, a slight difference in frequency will be measured for the different isotopes, called the isotope shift

$$\delta\nu^{AA'} = \nu^{A'} - \nu^A. \tag{1.33}$$

Two effects contribute to this shift: an effect related to the mass of the isotope, and one due to the extended charge distribution. These contributions are called, respectively, the mass shift and the field shift.

In the general calculation of a transition frequency between fine structure levels, the nucleus is assumed to be infinitely massive, relative to the orbiting electrons. Removing this assumption from the formalism means that the nucleus and electrons will orbit around the common center of mass, instead of around the nucleus. This means that the isotope shift will have a mass dependent part called the mass shift. The mass shift can be split further, but the analysis used in this work employed the King plot method (see Section 5.3). This method calculates the value for the mass shift directly, without any need for splitting due to different contributing sources.

The field shift originates from the fact that the nuclear charge distribution has a slightly different average radius for each isotope or isomer [19]. It can be expressed as a function of the change in mean square charge radius between two isotopes.

Putting together both of these effects, the final isotope shift, observed as the difference in the central transition frequency between two isotopes, can be written as

$$\delta\nu^{A,A'} = F\delta\left\langle r^2\right\rangle + \left(\frac{m\left(A'\right) - m\left(A\right)}{m\left(A\right)m\left(A'\right)}\right)M, \tag{1.34}$$

where $m\left(A\right)$ is the mass of the isotope with mass number A, and F and M represent sensitivity of the considered transition to the field and mass shift. The evolution of the mean square charge radius can reveal information about the nuclear structure. A sudden change in the slope indicates a shell closure or sudden onset of deformation.

Chapter 2

Collinear Laser Spectroscopy

Pew Pew Pew

<div align="right">Lasers in Star Wars</div>

The Collinear Laser Spectroscopy technique will be introduced in this chapter, going from the concepts behind the technique to the expected line shape of fluorescent decay. The setup used in the ISOLDE facility at CERN is also discussed, as are additional effects that contribute to the measured spectrum.

2.1 Technique

Because the hyperfine splitting is on the order of μeV, compared to electron transition energies of a order of eV, measuring this requires a high-resolution spectroscopic measurement technique. Collinear laser spectroscopy is an example of such a technique.

An ion or atomic beam is overlaid with a laser beam tuned to the chosen transition frequency. After the resonant excitation of the atom or ion beam, the ions/atoms decay from their excited state by emitting a fluorescence photon. These photons are detected through optical detection, by photo-multiplier tubes (PMTs). The neutralization cell, also called the charge exchange cell, neutralizes ions. This cell is only used if the transition to be probed is an atomic transition. In the case of an ionic transition, the neutralization cell is not used to neutralize the ions. It is still used for delivering an additional voltage to the beam (see further in the text for more details).
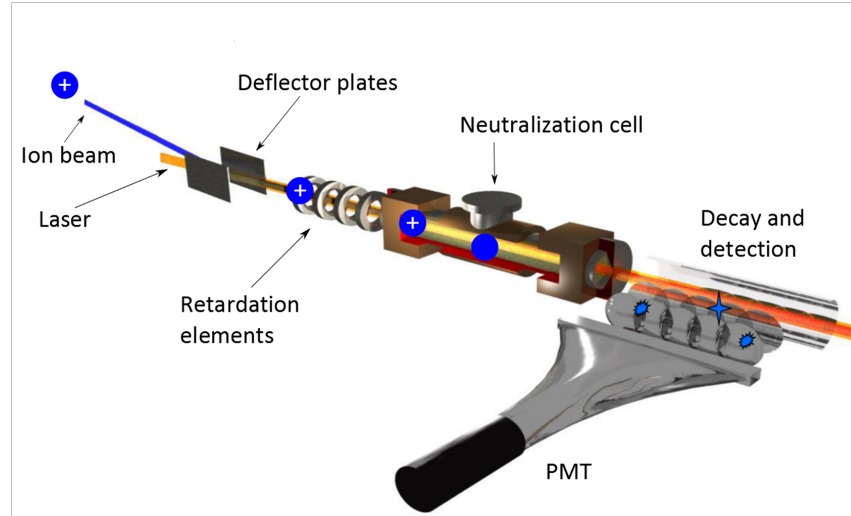
Figure 2.1: *The geometry of a collinear laser spectroscopy setup. Figure adapted from Ref. [23].*

2.1.1   Velocity compression and Doppler shift

The reason for the high resolution of this technique is the fact that it is performed on accelerated beams. Assume an initial spread δE in the kinetic energy of the beam, e.g. as a result of a thermal distribution of velocities. Since the laser frequency perceived by the atoms depends on its velocity through the Doppler effect, this energy spread results in broadening of the spectral lines. This broadening is called Doppler broadening. This δE still has the same value after electrostatic acceleration. The corresponding spread in velocity δv can be seen to decrease as the ion beam energy (and velocity) is increasing [21]:

$$E = \frac{mv^2}{2} \rightarrow \delta E = mv\delta v \rightarrow \delta v = \frac{\delta E}{mv}. \tag{2.1}$$

Thus, accelerating the beam decreases the spread in velocity, thereby reducing the Doppler broadening of the atomic transitions that are probed. With an acceleration voltage of roughly $40\,\mathrm{kV}$, the Doppler width is reduced by to a magnitude comparable to the natural line width of the hyperfine levels [22].

What remains to be done is scanning the laser frequencies in order to probe the different hyperfine transitions, which is observed through the emission of fluorescence photons after applying the correct transition frequency. Scanning the frequency region is normally not done by changing the laser frequency itself, since this is an instable process and technically challenging. However, controlling a voltage is much

easier. By changing the applied voltage, the speed of a charged particle can be changed. As a consequence, the Doppler effect also changes the perceived laser frequency. In such a collinear geometry, the formula for the Doppler shift is given by[†] [19]

$$\nu_{exp} = \nu_{trans}\sqrt{\frac{1-\beta}{1+\beta}}, \tag{2.2}$$

with

$$\beta = \sqrt{1 - \frac{m^2c^4}{(mc^2 + qV_{tot})^2}}. \tag{2.3}$$

Here, ν_{exp} is the perceived frequency, ν_{trans} is the frequency of the laser beam, m is the mass of the particle of interest, c is the speed of light, q is the elementary charge and V_{tot} is the total applied voltage. For the mass of the atom, the values as tabulated in the atomic mass table are used [24].

2.1.2 Line shape

The expected line shape of a resonant process, regardless of its origin in classical or quantum physics, is described by the Lorentzian line shape:

$$\mathcal{L}(x; \mu, \sigma, I) = \frac{I}{\pi} \frac{\sigma}{(x-\mu)^2 + \sigma^2}, \tag{2.4}$$

with μ the central resonance frequency and 2σ the full-width at half max. However, for this line shape to emerge, all broadening effects have to be homogeneous [25]. That is, these broadening effects must affect each atom in the beam in the exact same way. A typical example of a homogeneous broadening effect is the lifetime of a state. Due to Heisenberg's uncertainty relation, the uncertainty on the energy of an excited state is inversely proportional to its lifetime.

When the broadening effects under consideration are different for each individual atom (so a slightly different resonant transition frequency is present in each atom), the expected line shape changes from a Lorentzian shape to a Gaussian shape [25]:

$$\mathcal{G}(x; \mu, \sigma, I) = \frac{I}{\sigma\sqrt{2\pi}} \exp\left[-\frac{(x-\mu)^2}{2\sigma^2}\right], \tag{2.5}$$

with σ such that the full-width at half max is given by $2\sqrt{2\ln 2}\sigma$. An example of a heterogeneous broadening effect is the Doppler broadening. Since a gas has a certain

---

[†]Although with a different sign in the numerator, the same formula applies for an anti-collinear setup.
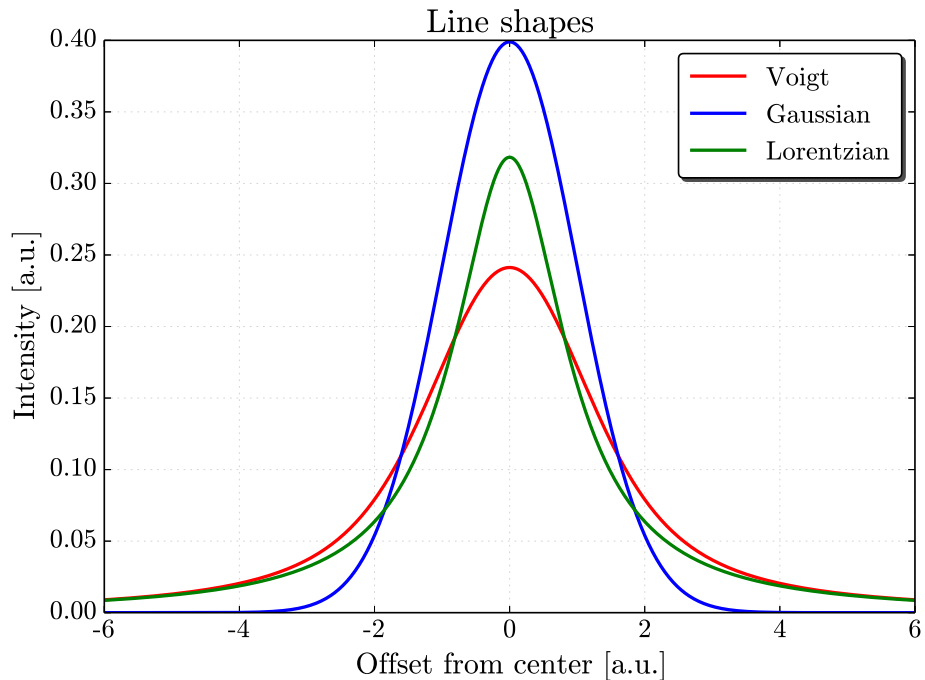
Figure 2.2: *The expected Lorentzian line shape is modified by the Gaussian line shape, resulting in the Voigt profile with a different width.*

temperature, the speed distribution is given by the Maxwell-Boltzmann distribution. This means that not all atoms have the same speed, the Doppler shift as experienced by each individual atom is different, and the broadening is heterogeneous and given by a Gaussian distribution.

The most interesting case, because it more closely resembles reality, is when both kinds of broadening effects are present. Both effects have to be taken into account, resulting in a convolution [25] of the Gaussian and Lorentzian parts:

$$\mathcal{V}(x; \mu, \sigma_L, \sigma_G, I) = I \int_{-\infty}^{+\infty} \mathcal{G}(x'; \mu, \sigma_G, 1)\mathcal{L}(x - x'; \mu, \sigma_L, 1)dx', \qquad (2.6)$$

where the width of the Gaussian and Lorentzian part can be different. The different line profiles are shown in Figure 2.2.

2.2 COLLAPS at ISOLDE, CERN

More than just the LHC, CERN also houses the ISOLDE facility, devoted to nuclear and solid state physics. A dedicated COllinear LAser SPectroscopy (COLLAPS)
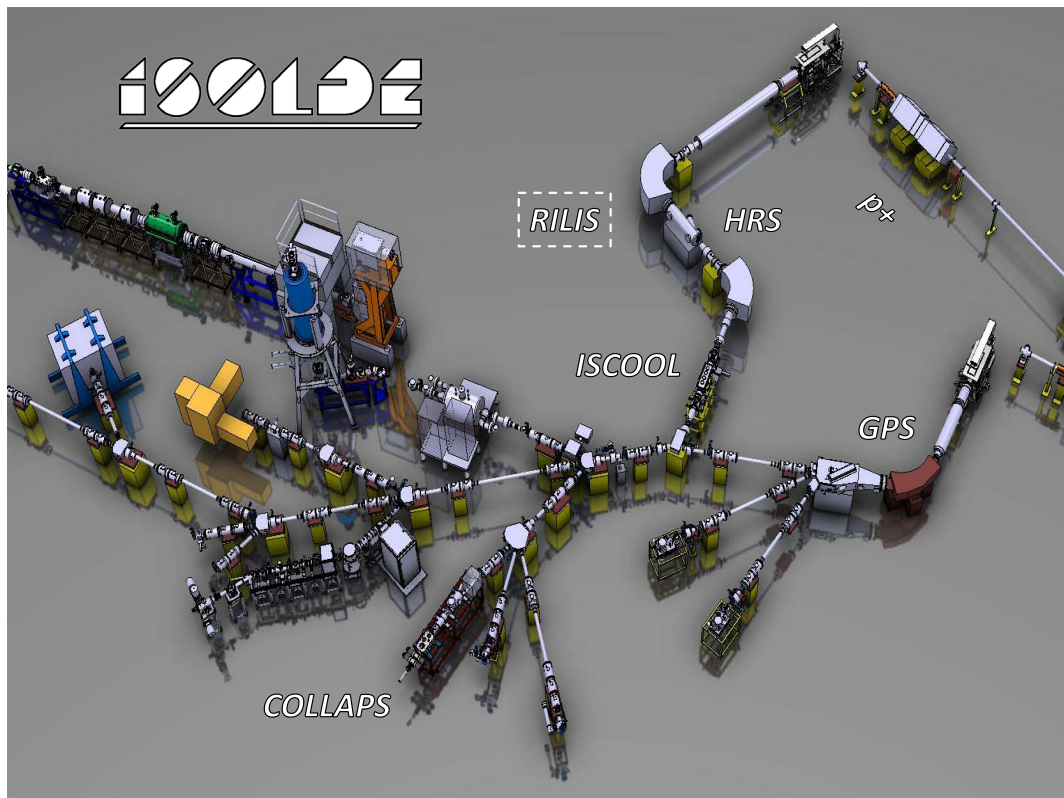
Figure 2.3: *Layout of the ISOLDE facility, with a focus on the COLLAPS setup. Courtesy of the ISOLDE website [26].*

setup is situated in this building. A proton beam impinges on a uranium carbide (UCx) target, creating different elements as a result of spallation, fragmentation and fission reactions. The Resonant Ionization Laser Ion Source (RILIS) ionizes the desired element, and the High Resolution Separator (HRS) mass separates for the desired isotope. The ion beam then passes through the ISCOOL RFQ cooler and buncher (see further in the text), then to the switchyard where the beam can be directed to the desired station. Figure 2.3 gives an overview of the beam line at ISOLDE, with a focus on those elements that are important to the COLLAPS setup.

2.2.1   Setup

The setup of COLLAPS itself is schematically drawn in Figure 2.4. The ion beam is deflected by the deflection plates on to a path collinear with the laser beam. The retardation elements and the neutralization cell produce a voltage which can slightly change the speed of the beam. This voltage is the scanning voltage as mentioned before. The optical detection system, marked with 6 in Figure 2.4, consists of four
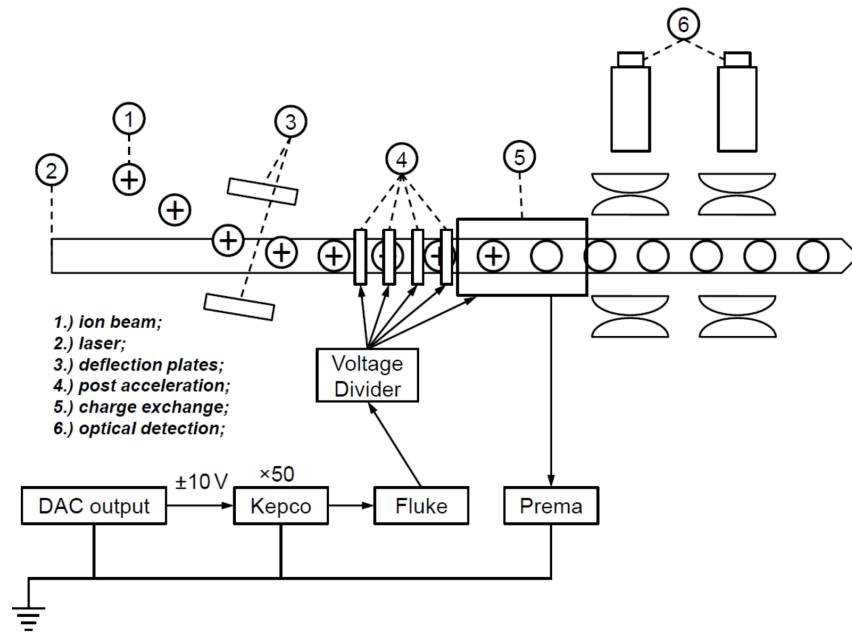
Figure 2.4: *Schematic drawing of the COLLAPS setup, taken from Ref. [19]. The scanning voltage (as applied by the DAC output) is divided among the retardation elements and the neutralization cell.*

PMT-tubes perpendicular to the beam axis, of which the count rate can be read in individually in the data acquisition system.

To give an idea of the dimensions of the setup, the distance between the neutralization cell and the first row of PMT-tubes in the COLLAPS setup is approximately 20 cm, with an additional 20 cm to the second row.

2.2.2   ISCOOL RFQ cooler and buncher

Using the ISCOOL RadioFrequency Quadrupole (RFQ) cooler and buncher gives a significant improvement of the measurement quality.

ISCOOL is a linear Paul trap which confines the ions in a small region in space. The potential barrier at the end of the trap is periodically dropped, so that a continuous ion beam is transformed into a bunched ion beam. In this experiment, the bunched beam had a delay of 50 ms between bunches, with a bunch width of 6 μs. This process is schematically illustrated in Figure 2.5a.

Trapping the ions in ISCOOL and releasing them in bunches has the advantage that the signal of the PMT tubes can be gated to only accept photons when the

(a)

(b)

(c)
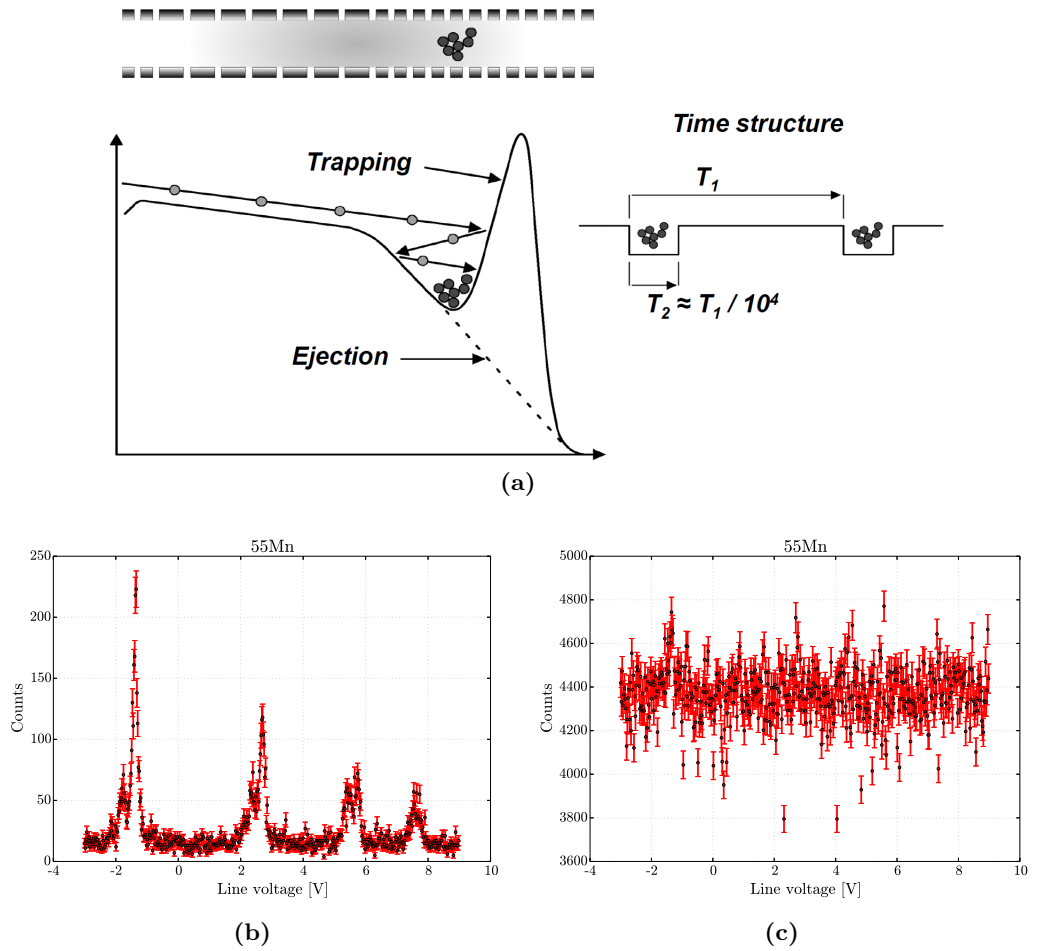
Figure 2.5: (a) *Periodically trapping the ions, and then ejecting them in a short time of typically a few microseconds, results in a bunched beam. In this experiment, there was 50 ms of time between bunches, with 6 µs bunches. Figure taken from Ref. [19].* (b) *Accepting only photons when the isotopes pass in front of the PMTs results in significantly better spectra then* (c) *accepting all photons.*

ions are passing in front of the optical detection station. The time window for this gating can be determined by time-of-flight measurements. See Figure 2.6 for a typical time-of-flight spectrum.

The result of this time gate on the photon signal, is that the background counts from scattered photons, which appear continuously due to the scattered laser light, are reduced by the ratio between the bunch width and the trapping time, which is about 10^4. Figures 2.5b and 2.5c show the difference between the gated and non-gated signals: while the hyperfine structure is very clearly visible in the gated spectra, the background photon counts are dominating the spectrum when no time-gating is applied, making hyperfine spectrum measurements impossible.
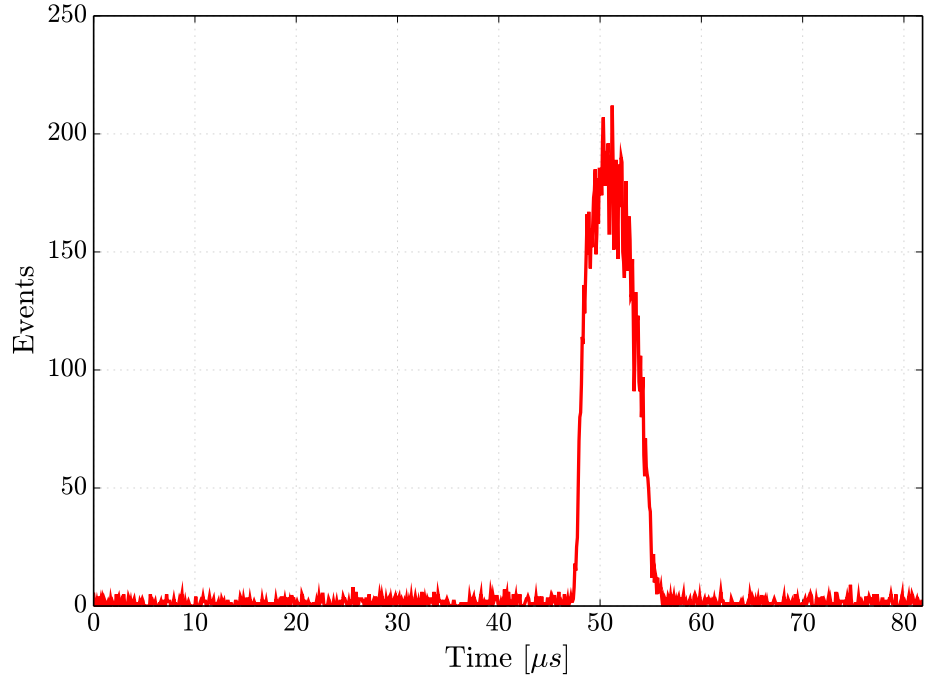
Figure 2.6: *The time-of-flight measurements showed roughly a 50 µs delay between the release from ISCOOL and the arrival in front of the PMTs.*

2.3   Neutralization cell

If the desired transition line is an atomic transition, the ions have to be converted to an atomic beam after all required voltages are applied. This neutralization of the ion beam takes place by inducing resonant charge exchange: the ion beam passes through a vapor of a suitable alkali metal (AM), which is easily ionized:

$$\text{Mn}^+ + \text{AM} \longrightarrow \text{Mn} + \text{AM}^+ + \Delta\text{E}. \tag{2.7}$$
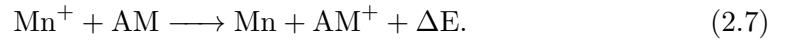
In this way, the ion absorbs the missing electron from the AM and becomes a neutral atom. Afterwards, spectroscopy on atomic transition lines can be performed. In the case of a resonant reaction, $\Delta E = 0$.

Additionally, a second process can take place in the neutralization cell, namely inelastic collisions with the vapor atoms. These collisions excite the atoms of the beam to a metastable state, meaning that colliding atoms lose energy:

$$\text{Mn} + \text{AM} \longrightarrow \text{Mn}^{\text{m}} - \Delta\text{E} + \text{AM} \longrightarrow \text{Mn} - \Delta\text{E} + \text{AM} + \text{h}\nu. \tag{2.8}$$
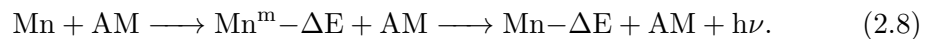
Since this collision excites to a well-defined state, the energy loss is the same for all affected atoms, which means that this process induces a general shift of the entire spectrum.

When the energy of this meta-stable state is determined, the energy loss can also be incorporated in the data analysis, as a side-peak that appears as a left tail on each hyperfine transition peak. The energy in eV can be directly converted to a decrease in voltage experienced by the atoms. If the state has an energy of $1\,\text{eV}$, the ions/atoms that collide once experience $1\,\text{V}$ less than the real applied voltage. This process can be repeated multiple times, with the probability of it happening n times given by the Poisson distribution [19]

$$P(n) = \frac{x^n}{n!} \exp\left[-x\right],\tag{2.9}$$

with each collision inducing the same decrease in voltage. Here, x is a parameter that depends on the physical parameters of the vapor, but which is usually left as a parameter in the fitting routine.

Part II

Motivation and experimental results

Chapter 3

Physics motivation

> The way to get started is to quit
> talking and begin doing.
>
> ———————————————
>
> WALT DISNEY COMPANY

Nuclear structure is preferably tested in the neighborhood of magic numbers because of the simple nature of these isotopes. The region around the apparent doubly magic $^{68}_{28}\text{Ni}_{40}$ (see Figure 3.1 for the relevant part of the nuclear chart and orbitals) is especially interesting. It has already been shown that the $N = 40$ shell closure is no longer present below $Z = 28$ [27]. The disappearance of this closure has been linked to the $\nu g_{9/2}$ orbital intruding in the pf-shell [28]. Shell model calculations in this region below $N = 40$ typically use an interaction such as GXPF1, where a hard $N = 40$ shell closure is assumed. The question is then when this description breaks down; when is the intruding orbital of sufficient importance to change the observables?

Also unknown are the spins of the ground states of several Mn isotopes, which can already reveal some information about the nuclear structure. A deviation from the spin predicted by the extreme single particle model is the first sign that additional interactions have to be considered.

3.1   Spin determination

In the manganese chain, all spins from ^{59}Mn onward are tentatively assigned spin $5/2-$ in the National Nuclear Database [29]. The spin assignment of ^{63}Mn is based
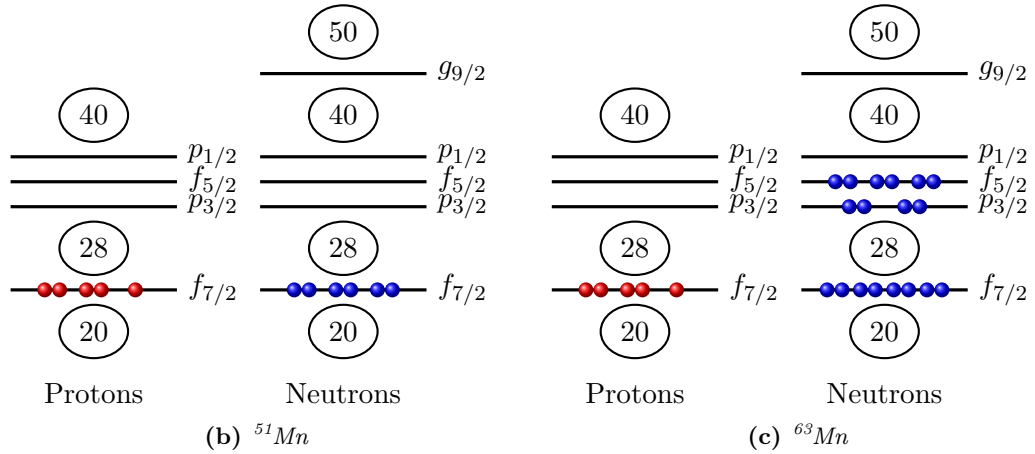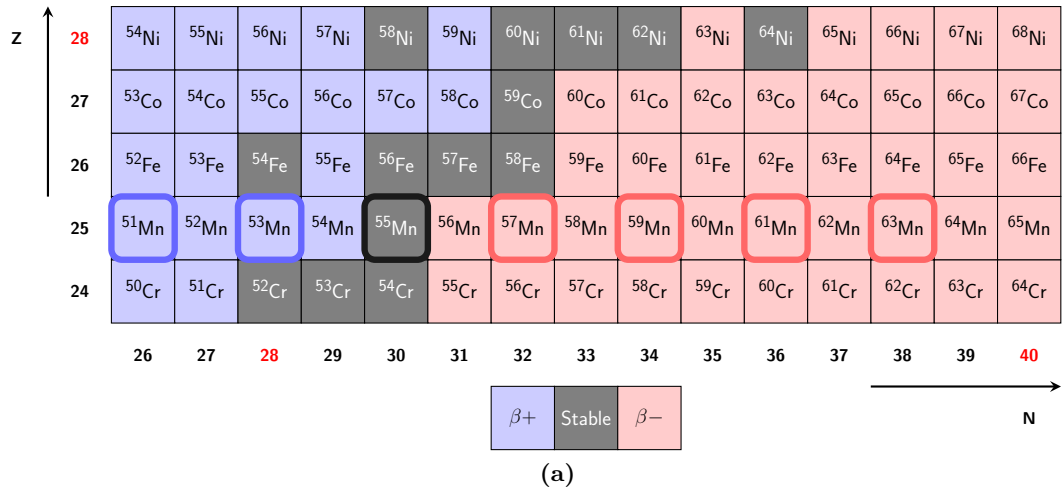
Figure 3.1: (a) *The part of the nuclear chart of interest. The decay mode is indicated, with the magic numbers indicated in red. The experiment measured the structure of Mn isotopes, from* (b) ^{51}Mn *up to* (c) ^{63}Mn*. The nuclei discussed in this work are bordered in a thick line. The shell model levels of interest are also pictured.*

on systematics, while ^{59}Mn and ^{61}Mn are assigned this spin using log ft-values measured in β-decay spectroscopy [30]. These spin assignments are then based on the tentatively assigned spins in the daughter states in Fe isotopes.

Spin determinations based on such indirect observables have to be handled carefully. A recent experiment on Ga [31] has shown the strength of collinear laser spectroscopy in this respect: the spin can be directly measured, based on the observed transition amplitudes and correlated positions. Comparing the number of observed transitions to the number predicted transitions for each possible spin already provides a first indication to discriminate between spin 0, 1/2, or 1 and higher spins. Intensity ratios, as provided by the Racah intensities, provide a second method to determine

the nuclear spin. The extracted nuclear moments also provide an indirect means to exclude certain spin options. Finally, the ratio between the upper and lower hyperfine parameters is also sensitive to the assumed spin, and can in some cases be used as well to determine the nuclear spin.

3.2   N=40 shell closure

The $N = 40$ shell gap is an oscillator shell gap, characterized by levels of opposite parity on either side, with the first level above this gap being the $\nu g_{9/2}$-level. The difference in parity prohibits 1p1h excitations, resulting in observables that behave as if $N = 40$ is a robust shell gap, although the energy difference between the upper pf-orbit and the $g_{9/2}$ orbit is not necessarily large [34]. This gap can be probed by looking at the excitation energy of the first 2+ excited state of even-even nuclei (see Figure 3.2a) around $N = 40$. This excitation energy is expected to show a significant increase if a shell gap is present. As can be seen in the figure, Ni shows this doubly magic behavior, while Fe and Cr do not. However, ^{68}Ni only appears as doubly magic for this observable; other observables, such as the two-neutron separation energy, lack the distinctive irregularity as expected for a doubly magic nucleus [35] (see Figure 3.2b). It is mainly due to the filling of the proton shell and the difficulty of exciting across an oscillator gap that gives this appearance of ^{68}Ni being doubly magic.

Ni, Fe and Cr are all even-proton nuclei. The rapid development of a changing nuclear structure that these nuclei exhibit can be further characterized by looking at an odd-proton nucleus, such as Mn. The combination of an unpaired proton with the increased space in the proton shell are expected to increase the importance of proton-neutron interactions. These interactions will have an effect on the population of the $\nu g_{9/2}$-level. The amount of neutrons needed on order for this level to be populated can be estimated from a comparison between experimental and theoretical data. We compare our data to theoretical calculations that do not take levels above $N = 40$ into account, because such interactions are not yet available for us. The comparison between experimental and theoretical data can pinpoint when these levels have a contribution in the ground state wave function. The magnetic moment is very sensitive to the exact wave function, and is thus a suitable observable for this comparison.
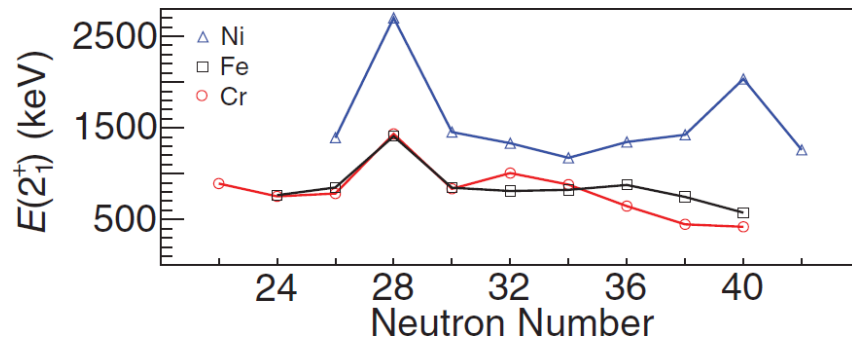
(a)
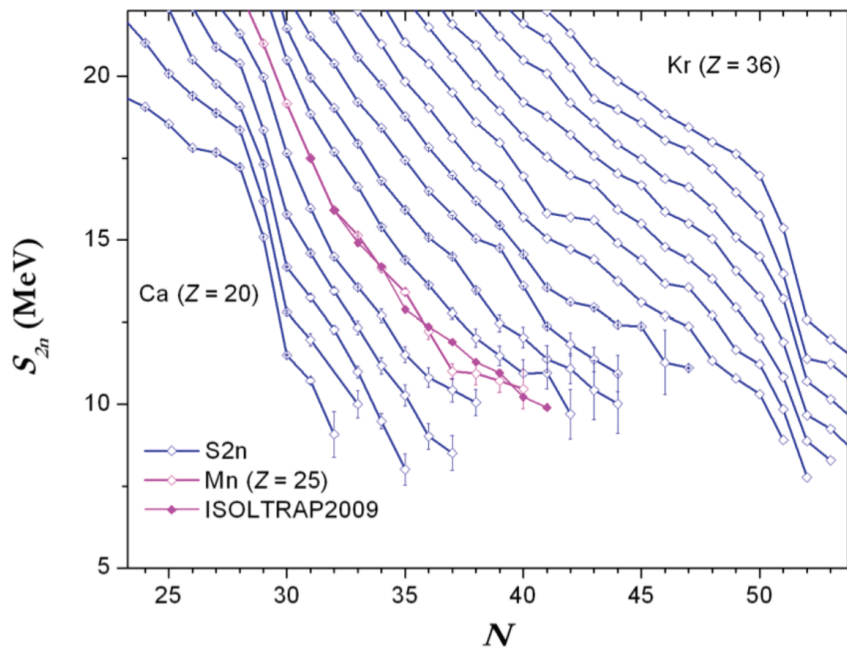
(b)

Figure 3.2: (a) *The excitation energy of the first 2+ state appears to indicate extra stability for Ni, but not for Fe or Cr. Figure adapted from [32]. (b) The two-neutron seperation energy in the neighborhood of Mn. N=40 does not show any significant extra binding in Mn or Ni, which would be visible as a sudden change in slope. Figure taken from [33].*

Chapter 4

Experiment and analysis

> It doesn't matter how beautiful your theory is, it doesn't matter how smart you are. If it doesn't agree with experiment, it's wrong.

<div align="right">RICHARD FEYNMAN</div>

The data from the odd-even isotopes gathered in the November 2012 run will be presented here, as well as the manner in which it was processed. The conversion from applied voltage to frequency is detailed, as is the fitting procedure and the used line shape. Data from the odd-odd isotopes has also been analyzed, but is only used in the King plot method.

4.1 Spectroscopic scheme

Originally, the experiment was proposed to use a new technique of optical pumping of the ion beam in the RFQ cooler ISCOOL (method explored at Jyväskylä [36]), in order to populate a metastable state from which efficient laser spectroscopy is possible with good sensitivity to both the magnetic and quadrupole moment. In this optical pumping scheme, ions are excited to a level at $230.5\,\mathrm{nm}$, which decays to a metastable state (see Figure 4.1a). From this state, the transition to the ground state is a forbidden M1 transition, resulting in a long lifetime. This allows transport of the metastable state to the COLLAPS beam line for laser spectroscopy from the metastable state.
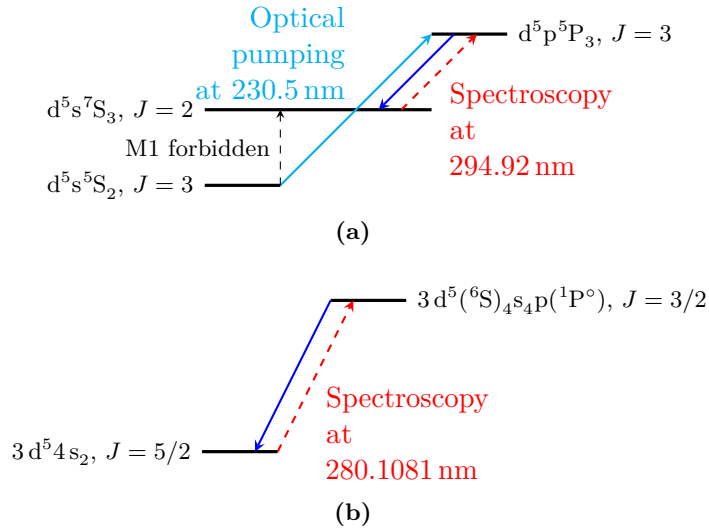
Figure 4.1: (a) *The original spectroscopic scheme used optical pumping to an excited state, which decays to a state where the M1 transition to the ground state is forbidden. Note that these states are ionic states.*(b) *The used scheme is a transition from the ground state to a state at 4.43 eV. The laser is tuned to 279 nm, very near to this transition energy. Note that these states are atomic states.*

However, the final experiment did not use this optical pumping scheme, but instead used spectroscopy from the atomic ground state to a 280.1081 nm excited state, as seen in Figure 4.1b. The reason for the change in plans was that optical pumping could not be achieved due to a misalignment in the ion cooler/buncher, which has only been observed for the first time during this experiment.

A summary of the known properties of the isotopes can be found in Table 4.1.

Table 4.1: *Ground state properties of the studied Mn isotopes which were known before the experiment.*

Isotope	N	Spin	Half-life	Magnetic moment $[\mu_n]$	Ref.
^{51}Mn	26	5/2−	46.2 min.	3.5683(13)	[29, 37]
^{53}Mn	28	7/2−	3.74 megayears	5.035(1)	[29, 38]
^{55}Mn	30	5/2−	-	3.4687179(9)	[29, 39]
^{57}Mn	32	5/2−	85.4 s.	-	[29]
^{59}Mn	34	(5/2−)	4.59 s.	-	[29]
^{61}Mn	36	(5/2−)	0.67 s.	-	[29]
^{63}Mn	38	(5/2−)	0.75 s.	-	[29]
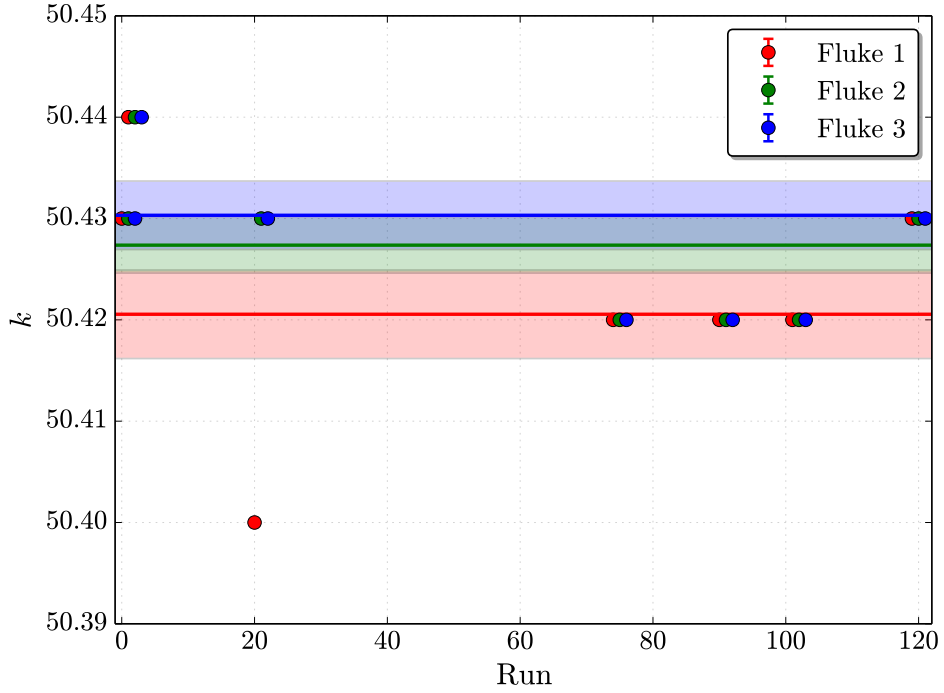
Figure 4.2: *The result of the Kepco calibration for the different Flukes at different times in the experiment. Each Fluke is associated with a different color, the circles representing the date points and the solid line the weighted average. The uncertainty on the average is represented by the shaded area. In all further figures, a solid line with a shaded area represents the weighted average with its uncertainty. For better visibility, the data points are offset from each other.*

4.2   Data processing

The raw data is collected as an array of counts observed in a detector versus the tuning voltage on the neutralization cell. For the analysis, the total voltage needs to be calculated and then converted to a frequency. Furthermore, not all spectra are suited for the final analysis because some scans were not intended for data taking, but only for localizing resonances before setting a dedicated scan range, so a selection has to be made.

The applied voltage can be calculated as

$$V_{tot} = V_{ISCOOL} - V_{PREMA} - k \cdot V_{line}, \tag{4.1}$$

The V_{PREMA} term is an isotope specific applied voltage that is read out through a voltmeter. The Fluke power supply, of which there are three, applies this voltage. The V_{line} is the scanning voltage, which can vary between $+10\,\text{V}$ and $-10\,\text{V}$. This signal

is amplified by the Kepco factor k, which is roughly 50. The exact value of k depends on the used Fluke power supply, so calibration scans are needed to determine the value of k. These scans are made periodically throughout the experiment. Figure 4.2 presents the calibration data for the different power supplies. The used power supply is also noted in each spectrum, allowing the use of the correct amplification factor.The ISCOOL voltage is explained in Section 4.2.1. For an illustration where the voltages are applied in the beamline, see Figure 2.4.

Taking this applied voltage, the Doppler shifted laser frequency observed by the accelerated beam can be calculated. Of course, this requires knowledge of the laser frequency itself. The frequency and power of the laser is automatically recorded every 0.2 seconds, which allows a very detailed view of the laser stability. By averaging over 2 seconds, to keep the amount of data manageable, a linear trend in the frequency is observed (Figure 4.3), with very small oscillations. The amplitude of these oscillations was investigated, and the uncertainty induced by it on the analysis results is 4 orders of magnitude smaller than the uncertainty of the fitting procedure. The stability of the laser frequency has been subdivided in different regions, based on visual inspection of the trend. For each of these regions, a linear fit was performed.

Also of note are the jumps present in the laser frequency. These never coincided with the measurement of a spectrum, and therefore had no effect on the results.

Combining both the calculated applied voltage and the laser frequency for each run, Eq. (2.2) is used to convert the voltage to the experienced frequency.

4.2.1   ISCOOL voltage and correction

The ISCOOL RFQ cooler and buncher, as explained in 2.2.2, re-accelerates the ion beam up to a certain voltage. This voltage can be read out and is manually recorded for the later data analysis. Over the course of the experiment, 65 entries were made in the logbook for the value of this voltage. This voltage, of the order of $40\,\mathrm{kV}$, can be approximated using a fitted spline, as shown in Figure 4.4. Alternatively, the time range was divided in regions based on the perceived trend in the ISCOOL voltage, and then a linear fit was performed in each region. The approach with the fitted spline eliminates the need for the subjective division in regions, allowing a more objective method for modeling the voltage.

Care has to be taken when using the spline method. The fit of the spline to the data has to be visually inspected, to ensure no false trend is detected by the fitting routine.
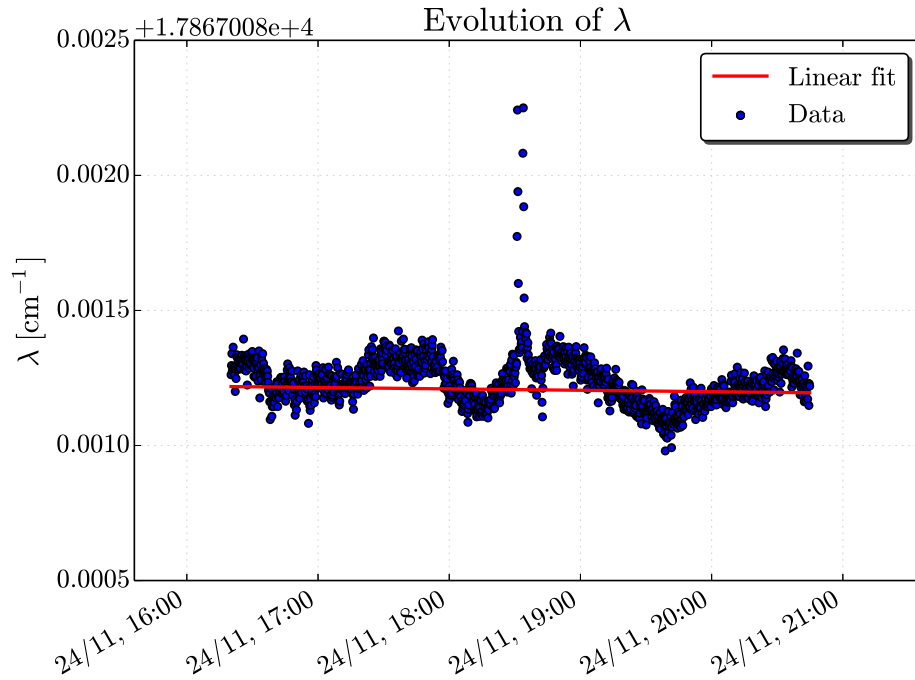
Figure 4.3: *A portion of the recorded laser frequency is presented here for clarity. The trend is clearly visible, as are the jumps in the frequency. These did not influence the measurements, as no measurements were being taken during this time. For better visibility, the data points in the figure are the average over 10 seconds instead of over 2 seconds.*

An additional correction has to be made, because the recorded value deviates from the true value. The recorded voltage is only accurate up to 0.2%, resulting in an uncertainty of 80 V which is too large for precision measurements [19]. Therefore we rely on a high-precision calibration of the voltage that was performed some time ago. Furthermore, from an experiment just before this one, the correction value could be estimated by comparing measured isotope shifts to published values for a series of stable Ca isotopes. Results for both -15.0 V and -15.5 V were compared, with the difference being within error bars. For the final analysis, we adopted a correction voltage of -15.0 V.

As can be seen in Figure 4.4, the deviation from the measurement can be, at most, 0.5 V. Since the uncertainty on the correction voltage had no effect on the result, neither does this uncertainty.
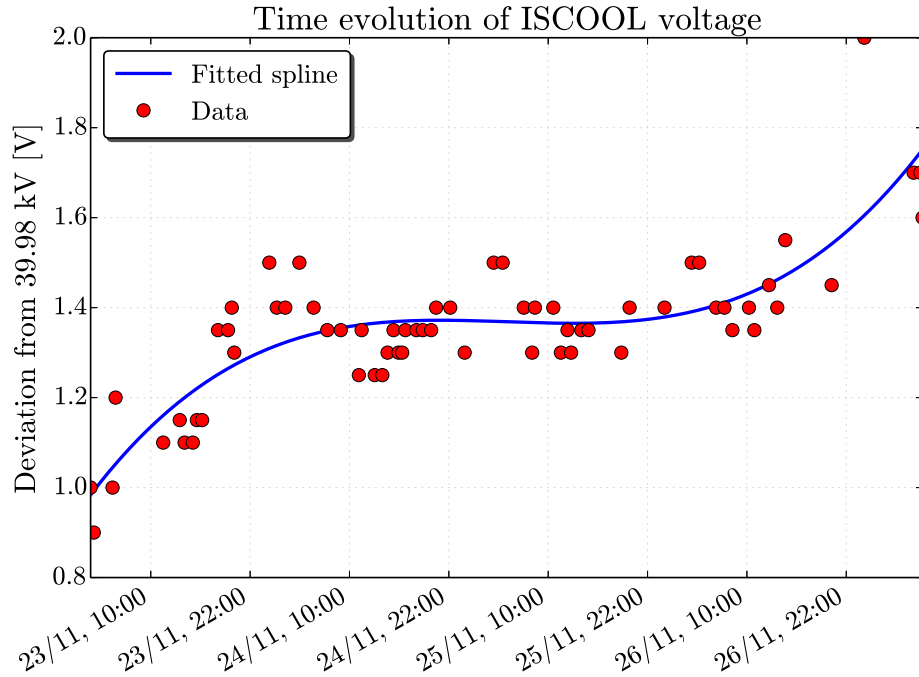
Figure 4.4: *The acceleration voltage of the ISCOOL RFQ cooler and buncher with the fitted spline approximation.*

4.2.2 Spectrum selection

During the experimental run, a total of 68 spectra on odd-even isotopes of Mn were taken. Of these spectra, 6 were so-called *go's* on another spectrum, meaning that the same region was scanned in the exact same way, and the collected data was added to the previous scan.

From the 62 independent spectra taken in the experimental run, not every spectrum is suited for further analysis. The quality of the spectrum is influenced by several external factors: the stability of the laser, the intensity of the beam, the scanned region, etc. E.g. some spectra which were used for locating the correct scanning region are automatically excluded from the analysis procedure, as these did not contain sufficient statistics in the full hyperfine structure range. Other factors do not automatically exclude spectra. For example, the stability of the laser would only have a noticeable impact if the frequency drifted over time, or scattered very wildly. Instability on a small timescale, or with a very small amplitude, will influence the spectrum in such a way that no hyperfine parameters can be extracted.

After assessing the quality of each spectrum, and eliminating those for a scan range determination, as well as the spectra whose deviation could be explained by external factors, 49 spectra remained. Table 4.2 summarizes how much spectra per isotope were kept for final analysis of the hyperfine parameters.

4.3   Analysis

Once the spectra are selected and converted, they can be fitted by a calculated spectrum, which is based on the nuclear and atomic spins, and hyperfine parameters. The location of the transitions in the spectrum is determined by the hyperfine parameters as in Eq. (1.29). Additional side-peaks have to be added to the fitting line shape to account for the collisions in the neutralization cell, as described in Section 2.3. The result is a spectrum as shown in Figure 4.5.

4.3.1   Fitting procedure

For the fitting, a wrapper for the FORTRAN library MINPACK written in Python was used. Each final fit was characterized by a number of free parameters:

A_{down}: the hyperfine A-parameter for the (atomic) ground state.

A_{up}: the hyperfine A-parameter for the (atomic) excited state.

B_{up}: the hyperfine B-parameter for the (atomic) excited state.

Center of Gravity: the shift of the entire spectrum from the transition frequency.

Table 4.2: *Summary of runs for each isotope, before and after spectrum selection.*

Isotope	# Independent Spectra	# Independent Spectra after selection
^{51}Mn	5	1
^{53}Mn	1	1
^{55}Mn	43	39
^{57}Mn	4	2
^{59}Mn	4	2
^{61}Mn	2	2
^{63}Mn	3	2
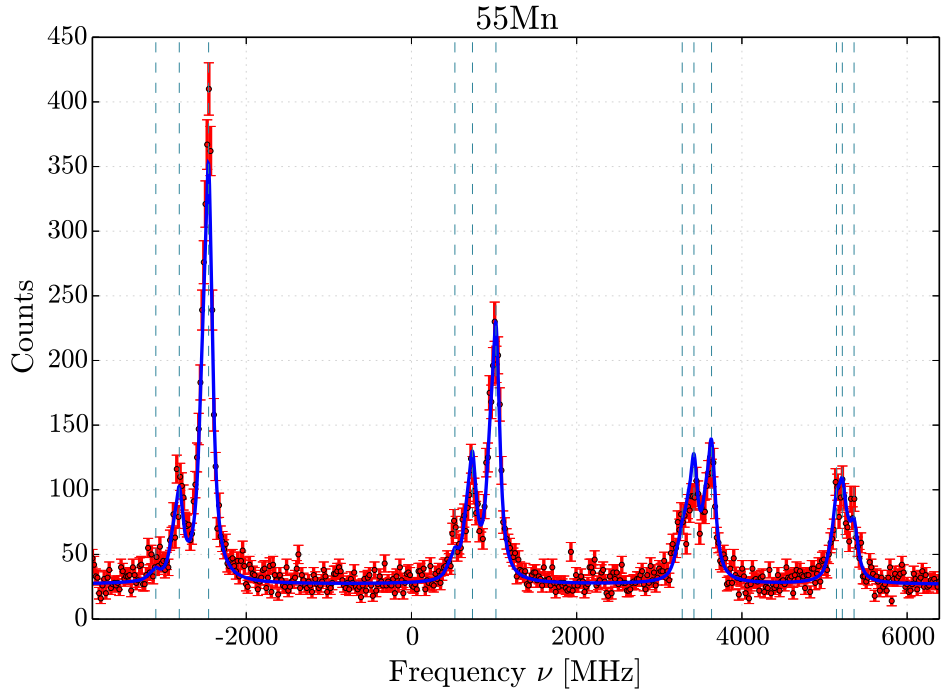
Figure 4.5: *A spectrum of ^{55}Mn is shown here as an example. The blue line is the best fit, with the thin lines indicating the position of a peak as determined by the fit.*

Amplitude: the intensity of the entire spectrum, related to the total amount of counts. The intensity of each individual peak was calculated using Racah intensities, as explained in Section 1.5.3.

Background: the constant background present.

η: the Lorentzian fraction of the used line shape (kept between 0 and 1). Further explanation will follow in Section 4.3.3.

Width: the width of each transition, related to the FWHM. This parameter was taken to be equal for all peaks. Only one width was used for both the Lorentzian and Gaussian contributions, see Section 4.3.3 for more information.

x: the Poisson factor for the collisions (kept between 0 and 1).

Before the final analysis, the collisional offset was left free, to have an indication to which states the collisions excited the ions. After analyzing the results, an average offset of 75 MHz was found, indicating collisions to a state with an energy of roughly 4.43 eV. This energy was then used to calculate the theoretical offset for each spectrum, and was fixed to this value in the final fit.

Other parameters influencing the shape of the fit are B_{down}, N (the number of collisions) and the collisional offset voltage. These last parameters are kept as constants: B_{down} was fixed to $0\,\text{MHz}$, a good approximation given the very small literature value, which is $0.024(4)\,\text{MHz}$ [37] for ^{55}Mn; N was kept at 1, <mark>assuming that the atoms only underwent 1 collision in the neutralization cell; and the collisional offset voltage was calculated for each separate run.</mark>

The MINPACK library minimizes a certain cost function in a least squares method. The cost function used is the chi-square function:

$$\chi^2 = \sum_{i=0}^{N} \frac{(x_i - \hat{x}_i)^2}{\sigma_i}, \tag{4.2}$$

with $\hat{x}$ the value as estimated by the fit. When this cost is minimized, errors on the used parameters are estimated using the estimated covariance matrix. The goodness of the fit is usually presented in the reduced chi-square:

$$\chi^2_{red} = \frac{\chi^2}{N - N_{var}}, \tag{4.3}$$

which is expected to be 1 in case of a good fit. When the value of this reduced chi-square is slightly greater, the errors on the parameters are enlarged by a scale factor

$$S = \sqrt{\chi^2_{red}}, \tag{4.4}$$

as explained on page 14 of the introduction of Ref. [40]. The reasoning is that a larger value indicates an underestimation of the errors, which propagates through in the final result.

4.3.2   Weighted average

When calculating the average of a series of measurements, the error on each individual value has to be taken into account, and a final error has to be given to the weighted average. Two sources contribute to this error: a *statistical* source, based on the error of the used measurements, and <mark>a *scattering* source, caused by uncontrollable variations in the experimental circumstances.</mark>

After the fitting is complete, the weighted average of a particular parameter is calculated as

$$\langle x \rangle_{weighted} = \frac{\sum_{i=1}^{N} \frac{x_i}{\sigma_i^2}}{\sum_{i=1}^{N} \frac{1}{\sigma_i^2}}. \tag{4.5}$$

The σ used in this formula corresponds to the error on the parameter as provided by the fitting routine.

For the statistical error, the well-known equation

$$\sigma_{stat}^2 = \frac{1}{\sum_{i=1}^{N} \frac{1}{\sigma_i^2}} \tag{4.6}$$

is used, while the scattering error is calculated using the formula for the weighted variance of a sample, given in Ref. [41] as

$$\sigma_{scatter}^2 = \frac{\sum_{i=1}^{N} \frac{\left(x_i - \langle x \rangle_{weighted}\right)^2}{\sigma_i^2}}{\left(1 - \frac{1}{N}\right) \sum_{i=1}^{N} \frac{1}{\sigma_i^2}}. \tag{4.7}$$

The final error on the weighted average is taken to be the maximal of both these values.

4.3.3   Used line shape

Considering that still some small non-homogeneous broadening of the line shape cannot be excluded, a Voigt profile cannot be excluded. Calculating a Voigt profile as expressed in Eq. (2.6) is resource-intensive. Therefore, the choice was made to use a pseudo-Voigt profile. Instead of a convolution of a Gaussian and a Lorentzian, the Voigt profile is approximated by using the formula given in Ref. [42]:

$$\mathcal{V}\left(x; \mu, \sigma, I, \eta\right) = \eta \mathcal{L}\left(x; \mu, \sigma, I\right) + (1 - \eta)\,\mathcal{G}\left(x; \mu, \sigma, I\right), \tag{4.8}$$

which is a weighted sum of a Lorentz and a Gauss profile. The η in this formula is the same η as explained in the list of parameters; as this parameter represents a percentual contribution of each line shape, this parameter is bounded between 0 and 1. Ref. [43] cites a deviation of 0.6% between the convolution and corresponding weighted sum.

In contrast to the full Voigt function, where the Lorentzian and Gaussian parts could have different widths, the pseudo-Voigt function does not allow this. A convolution produces a line shape that has a single associated width, while simple addition retains both widths.

4.3.4 Number of sidepeaks

Taking into account the possibility of collisions, a number of sidepeaks can be added to the spectrum. An increase in fit quality, as determined from the decrease in χ^2 toward 1, is observed by adding 1 sidepeak. The increase in quality by increasing the number of peaks from 1 to 2 is negligible. See Figure 4.6a for a visualization.

Furthermore, while a definite shift in center of gravity value is observed by including 1 sidepeak, this shift is not present by increasing the number of sidepeaks. Figure 4.6b presents evidence of this effect.

The hyperfine parameters do not experience this shift, which is normal. These only determine the relative position, while both the number of sidepeaks and the center of gravity have an effect on the absolute peak positions.

Since there is no significant difference in quality of the fit, or the obtained results, the final result is obtained by setting the number of sidepeaks to 1. This also has the additional effect of a faster convergence in the fitting routine.

Table 4.3: *Quantification of the hyperfine A-parameter of the upper state for different number of sidepeaks.*

Isotope	A $(N=0)$ [MHz]	A $(N=1)$ [MHz]	A $(N=2)$ [MHz]
^{51}Mn	$-994.6(1.8)$	$-994.4(1.8)$	$-994.4(1.8)$
^{53}Mn	$-998(3)$	$-998(3)$	$-998(3)$
^{55}Mn	$-962.1(1.7)$	$-962.6(1.8)$	$-962.9(1.8)$
^{57}Mn	$-966.9(1.8)$	$-967.2(1.7)$	$-967.5(1.6)$
^{59}Mn	$-970.2(1.4)$	$-970.5(1.4)$	$-970.8(1.4)$
^{61}Mn	$-980.6(1.4)$	$-981.1(1.3)$	$-981.5(1.2)$
^{63}Mn	$-956(3)$	$-956(3)$	$-956(3)$
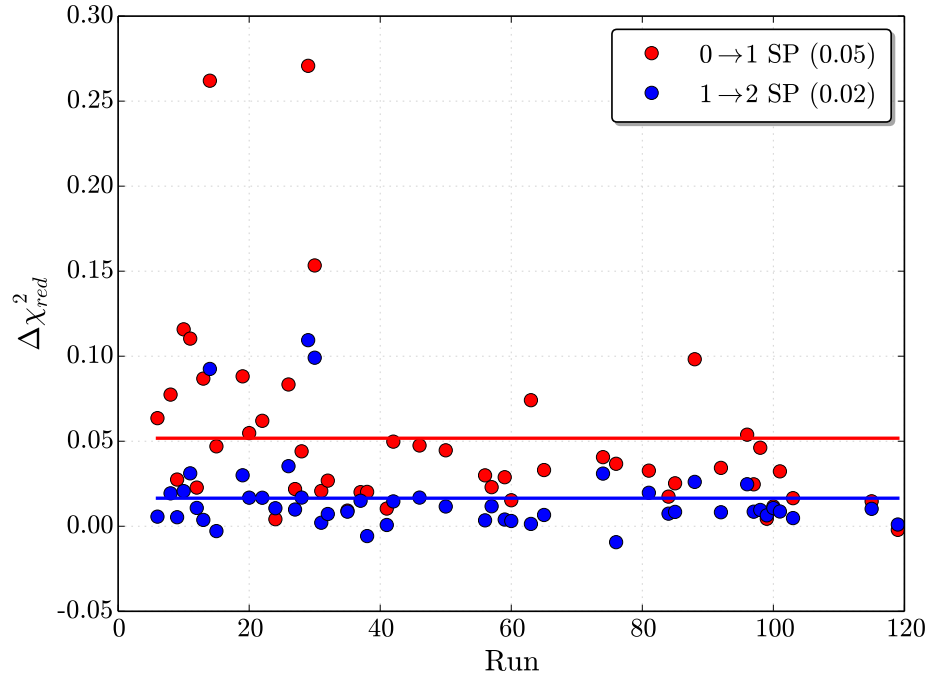
(a)
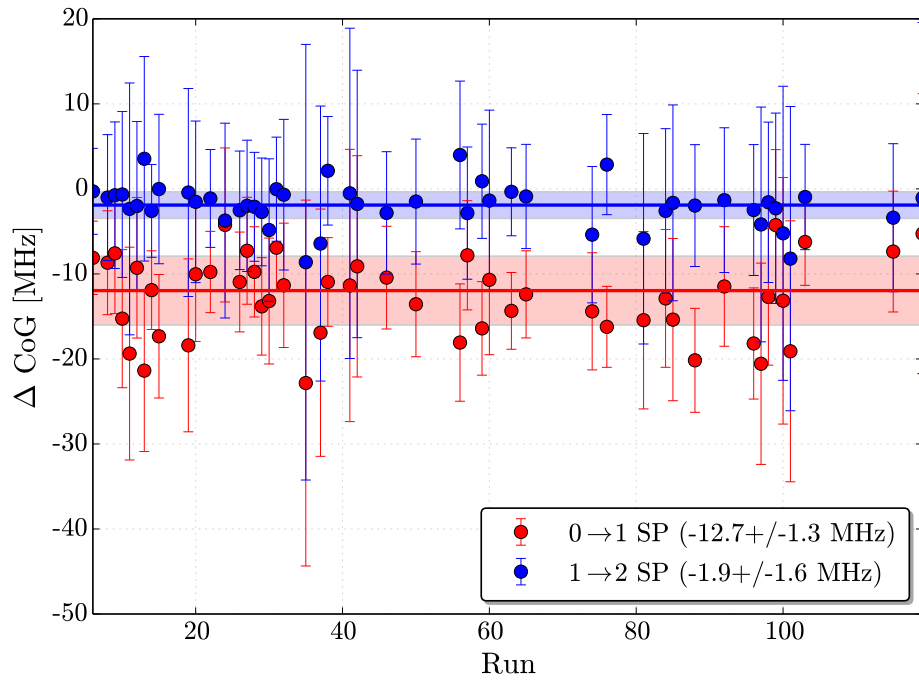
(b)

Figure 4.6: (a) *The change in χ^2_{red} is more present in the addition of one sidepeak (blue) than by adding two sidepeaks (green).* (b) *The change in center of gravity by adding one sidepeak is definitely noticeable. Going from one to two sidepeaks, the change is consistent with a value of zero, indicating that there is no real change.*

4.3.5 Fixing of parameters for fitting ^{51}Mn spectra

A note has to be made concerning the fitting of the spectrum for ^{51}Mn. Unconstrained fitting of the spectrum gave an A_{up}/A_{down} ratio that deviated from the ratio as calculated for the other isotopes (Table 4.4). Since this ratio should be the same for all isotopes (see Section 5.1), the ratio was fixed to 13.3 for ^{51}Mn, corresponding to the value given by the other isotopes. In Table 4.4 the g-factor extracted from A_{up} is compared to the literature value for the case of a restricted and unrestricted fit. It could be argued that the deviation of the ratio is only 1.5σ, which is not altogether that significant. However, such deviation is sufficient to lead to a wrong g-factor value.

4.4 Stability of parameters

The stability of the results as gathered from the spectra has to be investigated if possible. Only a few parameters should have the same value across different spectra: the Lorentzian factor, the Poisson factor, the width of the peaks and the hyperfine parameters.

4.4.1 Line shape

The Lorentzian fraction was bounded in the fitting routine to the region [0, 1], since other fractions do not make physical sense. The uncertainty as estimated by the program does not take these boundaries into account, and therefore extends beyond them. As can be seen in Figure 4.7, the line shapes are mostly Lorentzian in shape, with an average percentage of 95(6)%. Only one run (Run 88) has a more Gaussian shape, but the uncertainty on the result is fairly large. No explanation for this has

Table 4.4: χ^2_{red}, A_{up}/A_{down} and deviation of the g-factor from literature for the constrained and unconstrained fitting of ^{51}Mn.

	Constrained	Unconstrained
χ^2_{red}	1.87 (NDF=293)	1.86 (NDF=292)
A_{up}/A_{down}	13.3	12.7(4)
g-factor deviation	0.006(4)	0.014(7)
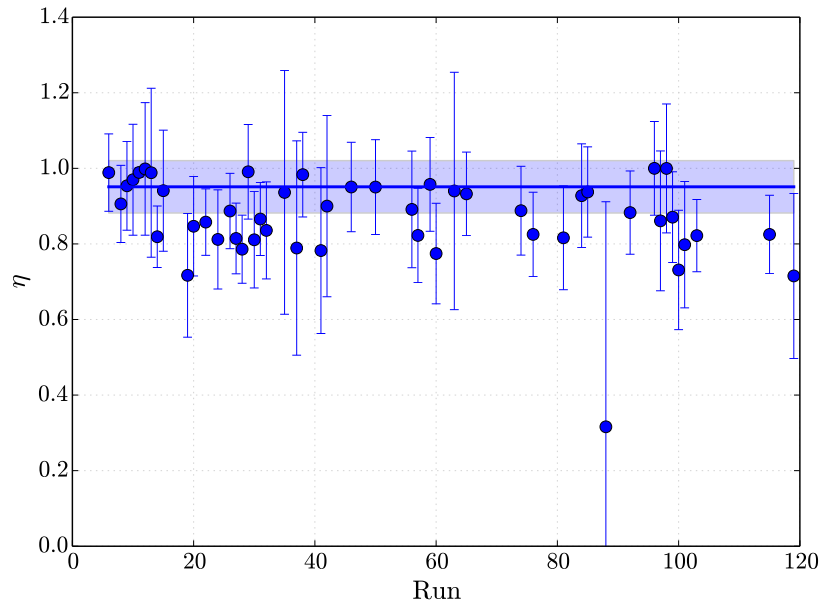
Figure 4.7: *In function of the run number, the Lorentzian fraction of the peaks does not vary much over the course of the experiment and is quite stable near 1.*

been found. Since the results of this run are consistent with those obtained from other runs, the run was not rejected for analysis.

Overall, due to the high percentage of Lorentzian shape present in the spectra, no significant deviation is expected if the chosen line shape would switch to a pure Lorentz shape.

The width of the peaks, as seen in Figure 4.8, does not deviate too much from a central value. Averaging gives a value of $61(5)\,\mathrm{MHz}$.

4.4.2 Poisson factor

The Poisson factor x is the ratio between the intensity of the primary peak and the first side peak. Since this process takes places within the neutralization cell where the conditions are stable during the entire experimental run, no significant trends or deviations are expected. Figure 4.9 gives an overview of the scatter on the found value. An average ratio of $0.24(9)$ is found, and the scatter around this value does not indicate large deviations.
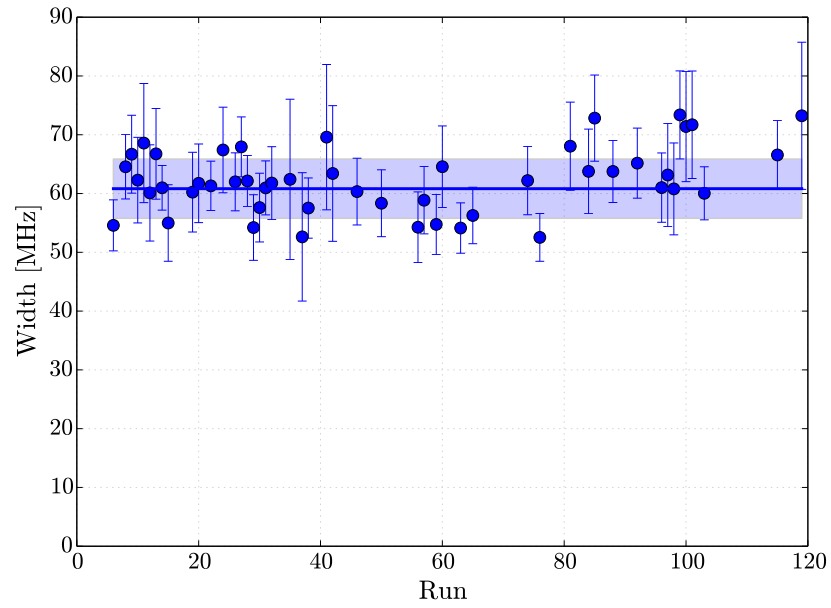
Figure 4.8: *In function of the run number, the widths of the transitions are shown. The values are fairly consistent, with no significant deviations or increase in uncertainty.*
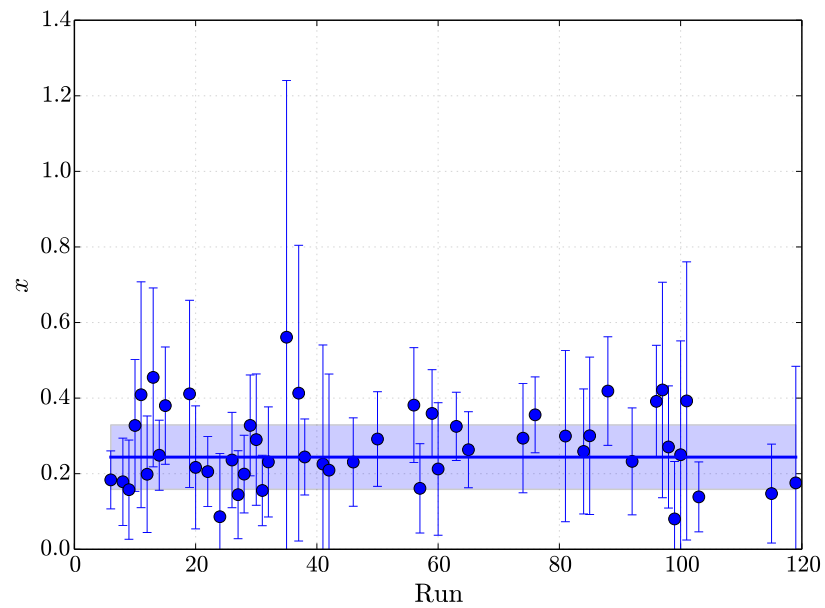
Figure 4.9: *The Poisson factor for each run is, as expected, quite stable.*
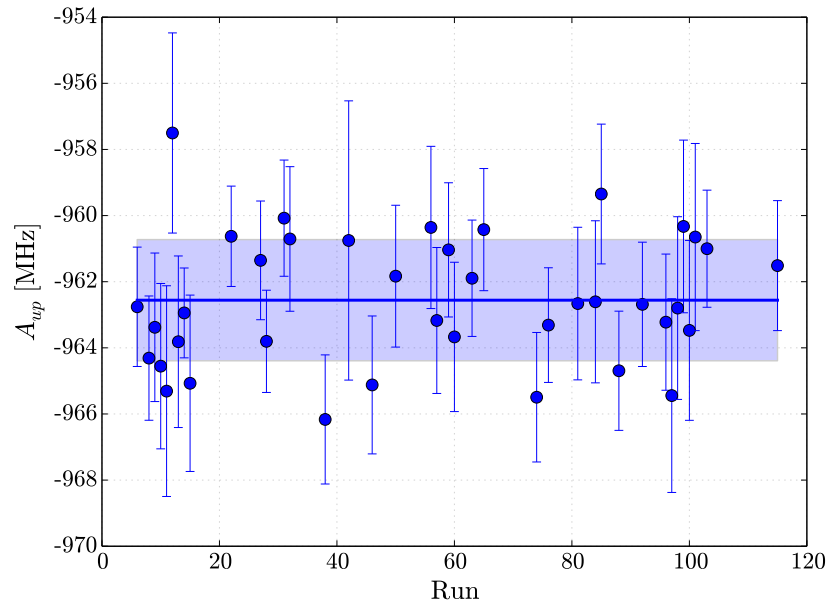
Figure 4.10: *The found value for A_{up} for the different runs is consistent. No abnormalities in the series of values is visible.*

4.4.3 Hyperfine parameters

While the stability of the previous Lorentzian and Poisson parameters was discussed for all isotopes, the stability of the hyperfine parameters will only be discussed for ^{55}Mn, and only for the upper state. Only ^{55}Mn has a sufficient amount of runs such that the stability can be discussed, since all other isotopes only have two runs at most, whose results lie within each others errorbar. The lower state has its B-parameter fixed to 0, and the A-parameter shows the same behavior for both states.

The stability of the A-parameter is well established by looking at the results in Figure 4.10. All but one of the measurements lies within 2σ, so no unusual deviations are present. The precision of the measurements is on the order of 0.2%.

The value of the B-parameter obtained by the analysis is not quite as precise (see Figure 4.11). The small quadrupole splitting results in a high relative uncertainty of the B-parameter, which carries through to the spectroscopic quadrupole moment. An uncertainty of at least 30% on the quadrupole moment does not lend itself well to an interpretation. The results as presented and discussed in Chapter 5 will therefore not include the quadrupole moments.
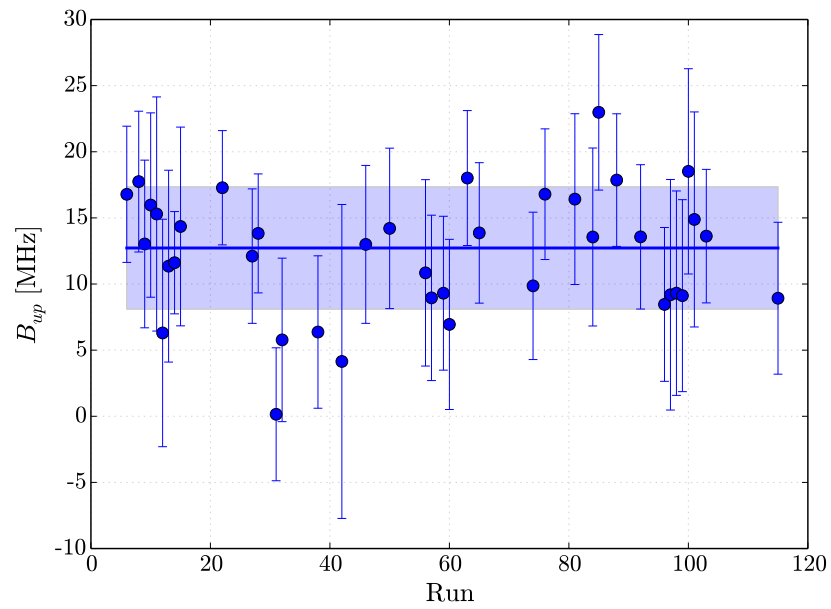
Figure 4.11: *The B_{up} parameter shows larger uncertainties, prohibiting the use of the resultant quadrupole moments in the interpretation.*

Chapter 5

Results

Using the analysis procedure as explained in Chapter 4, the spin and g-factor for the Mn isotopes are extracted. The spin is determined by the number of transitions in the spectrum and from the value of the B-parameter, while the g-factor is extracted from the fits to the spectra. After the calculation of the values, the g-factors are interpreted.

Note that, although the relative uncertainty on the quadrupole moment does not allow for any interpretation of these results, the values differ enough to use these in spin assignments.

5.1 Spin determination

For ^{59,61,63}Mn, the nuclear database [30] lists $I = (5/2)$ as assigned spin. In order to definitively assign a nuclear spin, spin values of 3/2, 5/2 and 7/2 were used in the analysis.

Considering the hyperfine transitions, as depicted in Figure. 5.2, the amount of spectral lines that will be seen is different for these spins. Taking into account that

(a) $I = 3/2$

(b) $I = 5/2$

(c) $I = 7/2$
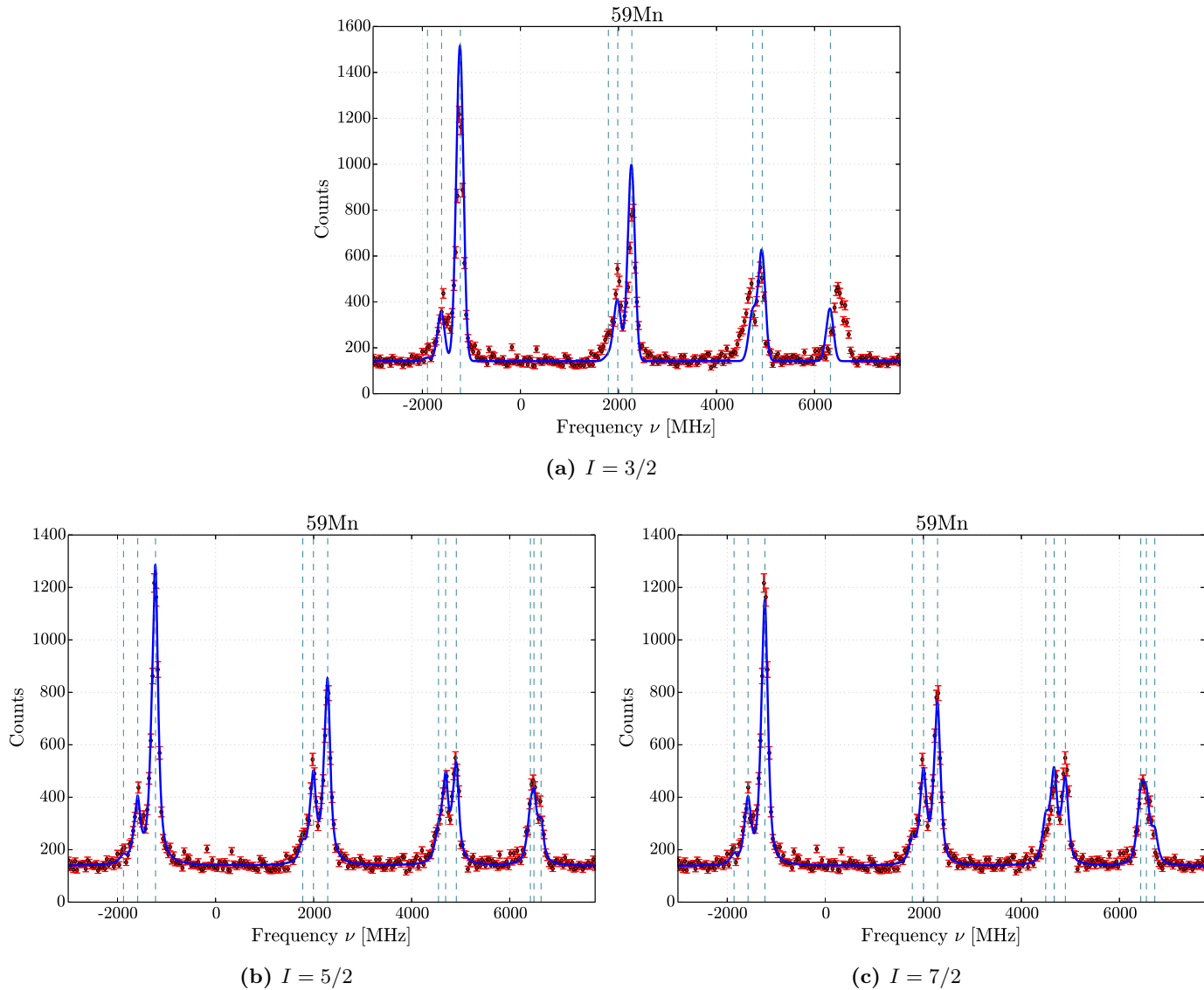
**Figure 5.1:** *The fitted spectra for ^{59}Mn, with the position of the peaks indicated with a thin dashed line. As can be seen in these fitted spectra, $I = 3/2$ clearly misses structure in the rightmost multiplet, while $I = 5/2$ and $I = 7/2$ fit equally well. The fits as presented here are also representative of the fitting for $^{61,63}Mn$.*

the excited state has a greater hyperfine splitting than the ground state, the spectrum for $I = 5/2$ and $I = 7/2$ is expected to show 4 multiplets of 3 peaks each, while $I = 3/2$ would feature 2 triplets, 1 doublet, and 1 single peak. The recorded spectra do not show doublets or single peaks, and do correspond with 4 triplets. Therefore, $I = 3/2$ can be excluded as a possible value.
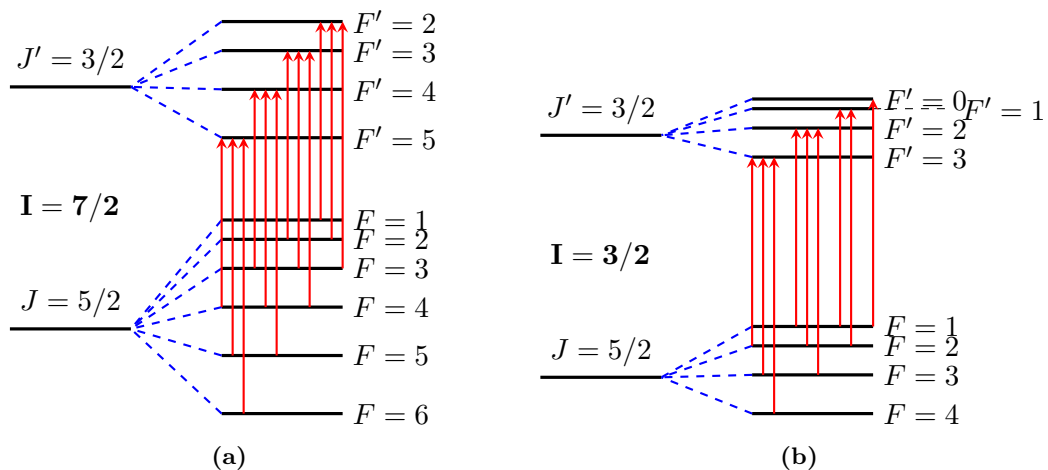
Figure 5.2: (a) *In the case of a nuclear spin $I = 7/2$, 12 transitions are possible, grouped per three. The same grouping can be seen for $I = 5/2$, as in Figure 1.7.* (b) *If the nuclear spin is only $I = 3/2$, 9 transitions will be seen.*

Since $I = 5/2$ and $I = 7/2$ give the same amount of transitions, the full analysis will have to be carried out with both values. As can be seen in Figure 5.1, the visual quality of the fit for both possible spins is satisfactory. The extracted moments do indicate a preference, however.

The value of the B-parameter obtained in both fits excludes $I = 7/2$ for all three isotopes. Fitting the data with spin $I = 5/2$ gives a B-parameter in the order of magnitude of 10 MHz for ^{59,61,63}Mn, consistent with the B-parameters of the other isotopes. Using $I = 7/2$ results in a value of roughly -200 MHz, more than an order of magnitude larger.

Converting this to observed quadrupole moments, the assumption of spin $5/2$ gives a quadrupole moment in the region of 0.5 eb, while spin $7/2$ adjusts this to ≈ -6 eb (see Figure 5.3). Since this region of the nuclear chart has a typical quadrupole moment that is smaller than 1 eb [44], $I = 5/2$ can be assigned to these three isotopes.

5.2 g-factors

The g-factor can be calculated from the A-parameter from either the upper or the lower state. Since the A_{up}-parameter had the smaller relative error, the g-factors are
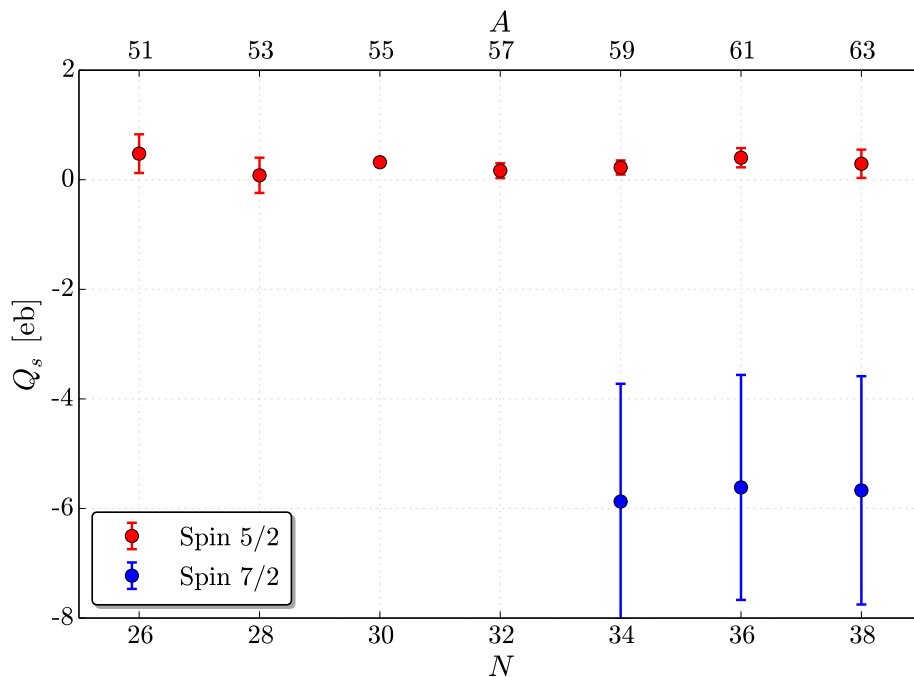
Figure 5.3: *The extracted quadrupole moment for spin 5/2 is consistent with the rest of the data and the quadrupole moment of other isotopes in the region. Spin 7/2 gives unusually high values, and can thus be excluded as a spin assignment.*

derived from the upper state. The exact formula used is

$$g_i = \frac{A_{up,i}}{A_{up,ref}} \frac{\mu_{ref}}{I_{ref}}, \tag{5.1}$$

with the reference isotope being ^{55}Mn. Since the hyperfine parameters of the excited state of ^{55}Mn could not be found in literature, the A_{up} parameter found for ^{55}Mn in this experiment was used. This means that no new experimental *g*-factor value for ^{55}Mn is established. The spin of ^{55}Mn is 5/2, and the magnetic moment is $\mu = 3.46871790(9)$ [44]. Calculating the *g*-factor of ^{55}Mn from the lower state leads to a result of 1.38(2) corresponding to $\mu = 3.45(5)$, so we see a good agreement between experiment and literature. An overview of the results is given in Table 5.1, with Figure 5.4 giving visual support.

The experimental value of ^{51}Mn found in this work deviates slightly from the literature value, although it is within agreement with our error bar. This deviation is probably due to our single viable spectrum for ^{51}Mn, where the analysis method also had to be slightly adjusted (see Section 4.3.5).
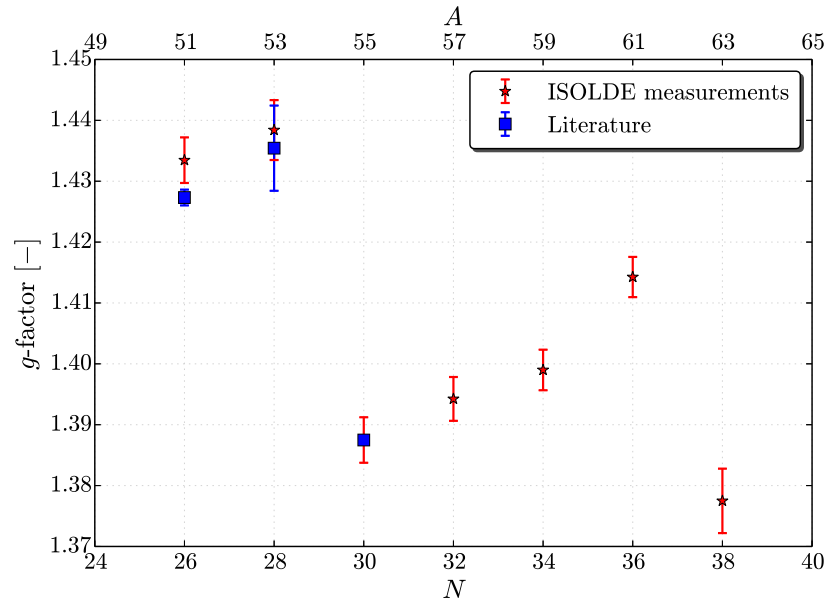
(a)
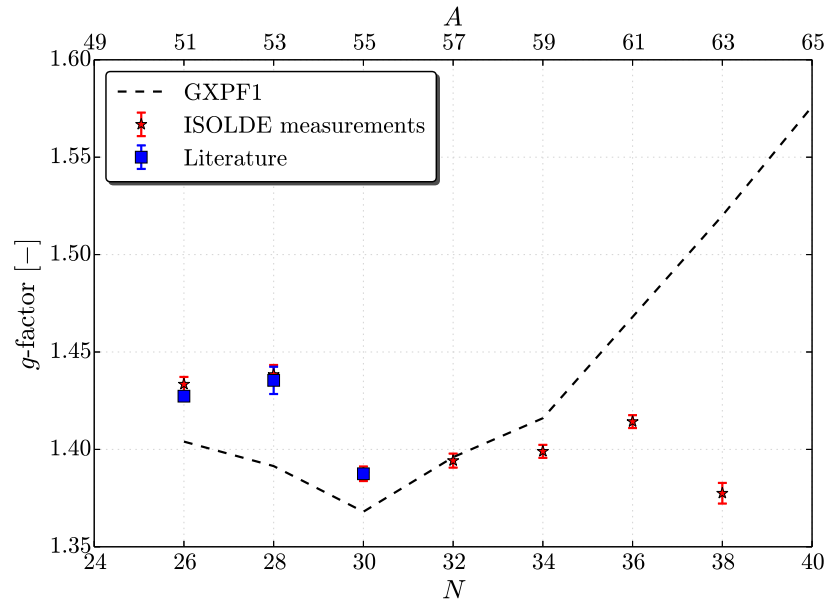
(b)

Figure 5.4: (a) *Comparison between the new results and the literature values as given in Refs. [37–39]. (a) The results of the new g-factor measurements, along with the literature values and the GXPF1 model predictions.*

The theoretical model to which the data will be compared is the GXPF1 model. This model takes an inert core of $^{40}_{20}\text{Ca}_{20}$, with the full pf-shell consisting of the $f_{7/2}$, $f_{5/2}$,

$p_{1/2}$ and $p_{3/2}$ orbitals as the model space. The effective g-factors have been adjusted to typical values for pf-shell nuclei: $g_s^{eff} = 0.9g_s^{free}$ for both protons and neutrons, and $g_\ell = 1.1$ for protons, $g_\ell = -0.1$ for neutrons. The effective charges are set to $1.3e$ for protons and $0.5e$ for neutrons [46].

The g-factors calculated by the GXPF1 model agree reasonably well with the experimental data (within 4%) up to $N = 34 - 36$. The increase in g-factor for $N = 36$ is overestimated by the model, while the observed decrease for $N = 38$ is not present in the calculation. Especially these last few values are of interest, because they indicate that the model space is not large enough.

The necessity of extending the model space implies that the higher lying levels have a non-negligible contribution. From this it can be concluded that $N = 40$ is not a shell closure.

### 5.2.1   Nilsson interpretation of results

The results can be explained and interpreted in a very intuitive way by applying the Nilsson model. This model is also used in the interpretation of energy levels of odd-odd Mn isotopes, but in the context of a projected shell model. For more information, see Ref. [47]. For Mn isotopes, calculations such as tabulated in Ref. [48] predict a positive sign for the deformation parameter. Values in this reference vary between 0.1 and 0.3 for the isotopes studied in this work.

The first observable on which the Nilsson model can shed some light is the evolution of the spin. The Mn isotopes have 25 protons, meaning they have three holes in the $Z = 28$ shell. The $\pi f_{7/2}$ orbital is thus occupied by five protons, so in the extreme single particle shell model a $7/2-$ ground state spin is expected for every odd-even

Table 5.1: *Overview of measured and calculated g-factors. The calculated g-factors are obtained by using the GXPF1 model, the literature values are taken from Ref. [45].*

	^{51}Mn	^{53}Mn	^{55}Mn	^{57}Mn	^{59}Mn	^{61}Mn	^{63}Mn
g (exp.)	1.434(4)	1.438(5)	-†	1.394(4)	1.399(3)	1.414(3)	1.378(5)
g (lit.)	1.4273(13)	1.435(7)	1.38748716(4)	-	-	-	-
g (calc.)	1.404	1.39143	1.368	1.396	1.416	1.468	1.52

†The literature value was used as a normalization factor, so there is no new data point for this isotope.
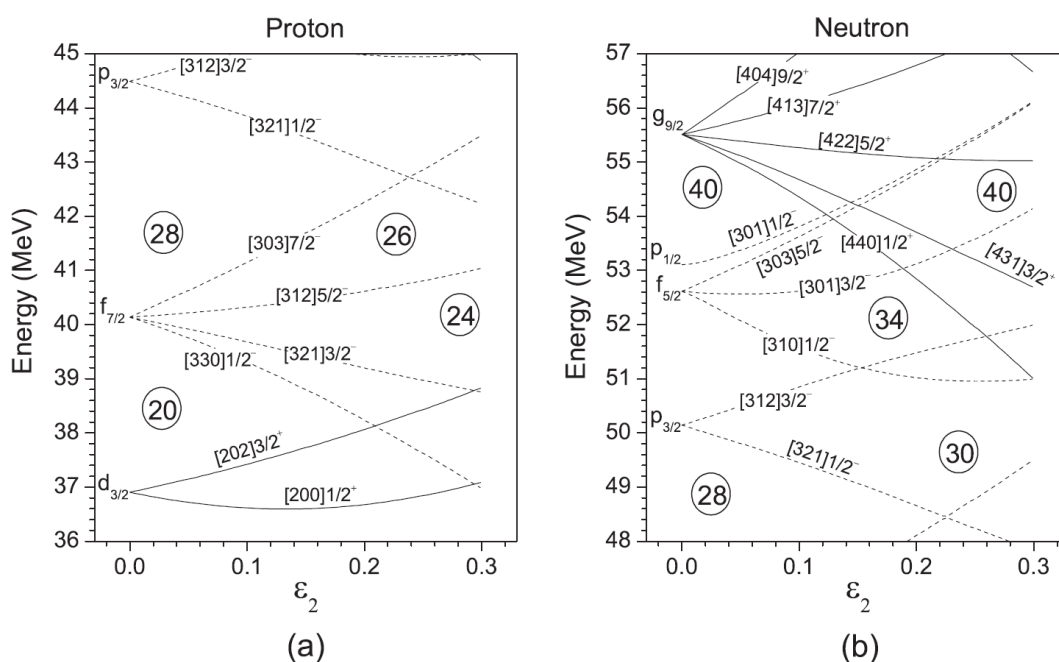
Figure 5.5: *The Nilsson levels for (a) protons and (b) neutrons relevant for Mn. Figure adapted from Ref. [47].*

Mn isotope. This expectation only holds for ^{53}Mn, which has a closed neutron shell at $N = 28$. It is clear that proton-neutron interactions with valence neutrons, available by removing or adding neutrons to $N = 28$, cause correlations that induce a change in ground state spin. Assuming a positive sign for the deformation parameter, the filling of the proton Nilsson levels automatically leads to a $5/2-$ prediction for the ground state spin, as seen in Figure. 5.5. This spin assignment can also be explained in the shell model as a seniority 3 configuration, where 3 protons in the $\pi f_{7/2}$ orbital are unpaired. In isotopes where deformation starts to develop, such configurations are known to become the ground state.

For the magnetic moment, the region of 0.1–0.2 as a value for the deformation parameter ϵ_2 is interesting. Here, the $g_{9/2}$-level in the neutron sector has been pulled down into the pf-shell orbitals. In this area, adding neutrons toward $N = 40$ facilitates excitations or even direct population of the $g_{9/2}$ orbital. This would immediately explain why the magnetic moments for $N > 36$ are not reproduced by the GXPF1 model, since the $g_{9/2}$ orbital is not taken into account in its model space. In this manner, the measurement of the g-factor indirectly suggests a deformation parameter of this approximate value.

Experimental values for the quadrupole moment would help in the further interpretation.While a small deformation is sufficient to get a seniority 3 shell model

configuration to become the ground state, a larger deformation between $0.1 - -0.2$ is required in the Nilsson model. A measurement of the deformation would help differentiate between the collective behavior as expected from the Nilsson model, and the shell model interpretation.

5.3 Charge radii

The charge radii can be calculated from the isotope shift, as given in Eq. (1.34). In order to do so, the field and mass shift factors F and M have to be calculated, and these are dependent on the transition used to measure the isotope shift.

The King plot method allows the determination of these factors from:

1. the isotope shift as measured in this experiment,

2. the calculation of the mass and field factors for another atomic or ionic transition [49].

Eq. (1.34) forms the basis of this technique. Label the two transitions with subscripts x and y, the quantity of interest is $F_x \delta \nu_x^{AA'} / F_y \delta \nu_y^{AA'}$. Rewriting this expression, the relation between the measured isotope shifts is [50]

$$\left(\frac{m(A) m(A')}{m(A') - m(A)} \right) \delta \nu_y^{AA'} = \frac{F_y}{F_x} \left(\frac{m(A) m(A')}{m(A') - m(A)} \right) \delta \nu_x^{AA'} + M_y - \frac{F_y}{F_x} M_x. \quad (5.2)$$

Since Ref. [45] includes calculations for the field and mass shift factors, and uses another transition than the 280.1081 nm line, fitting a straight line through rescaled isotope shifts allows the extraction of the field and mass shift factors for the 280.1081 nm transition. The rescaling of the isotope shifts is done by multiplying them by the mass factor in parentheses in Eq. (5.2). Figure 5.6 presents the King plot for the Jyväskylä data on the x-axis and the ISOLDE data on the y-axis.

From the King plot method, the field and mass shift factors for the 280.1081 nm transition are determined to be

$$F = -0.55(5) \, \text{GHz fm}^2, \quad (5.3)$$

$$M = 0.118(10) \, \text{THz u}. \quad (5.4)$$
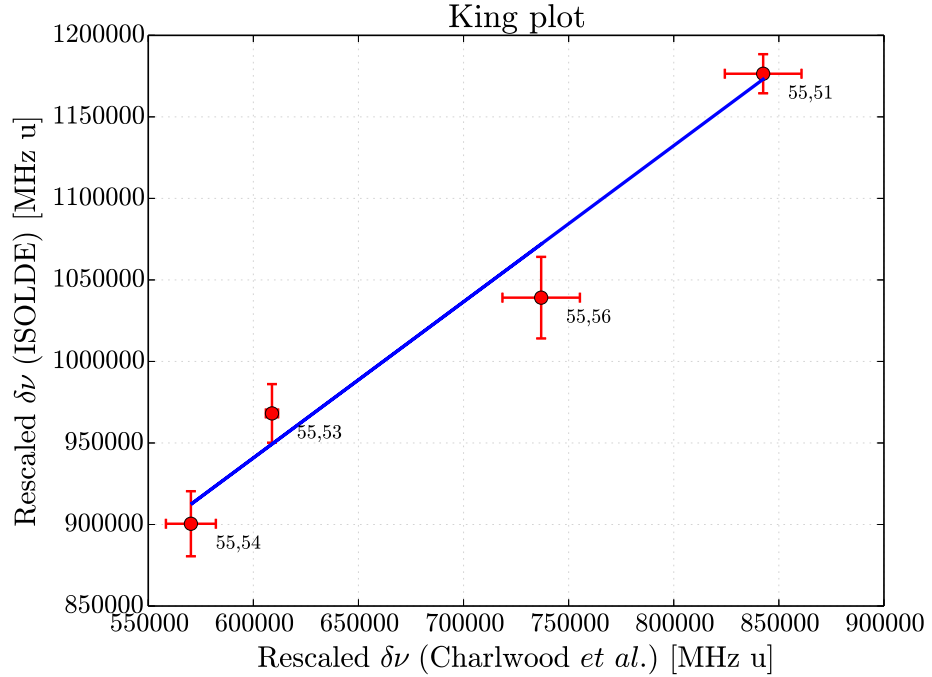
Figure 5.6: *The King plot, with the found isotope shift from the Jyväskylä data on the x-axis, and the ISOLDE data on the y-axis, both rescaled. The fit is moderately good, with a χ^2_{red} of 1.6 (NDF=2). For this plot, the spectra of the odd-odd Mn isotopes were also analyzed, but these results are not discussed in this work.*
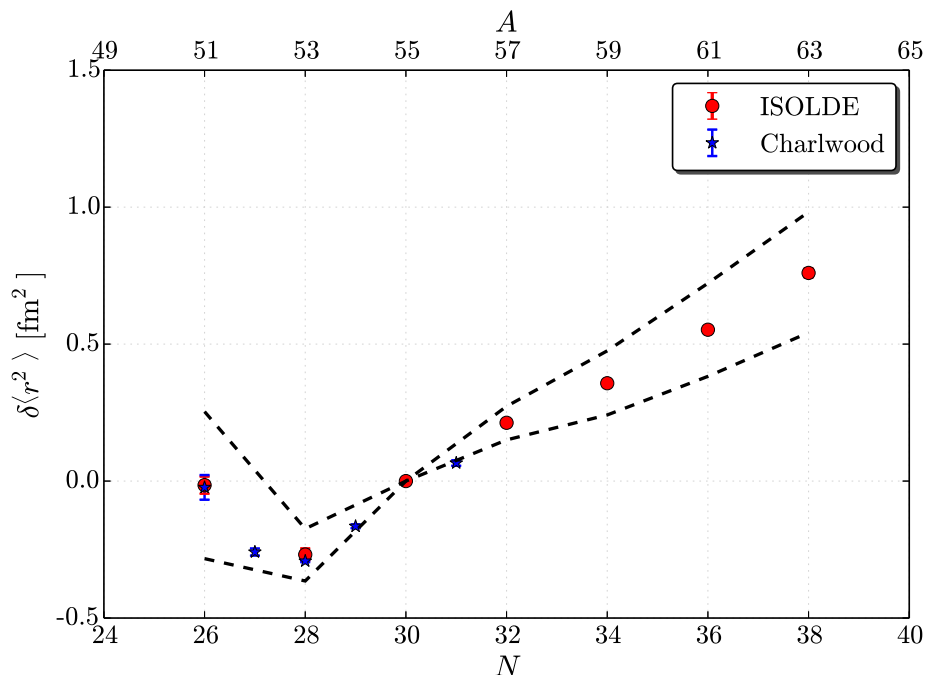
The difference in mean square charge radius can then be determined by using the formula

$$\delta \left\langle r^2 \right\rangle = \frac{\delta\nu^{\,^{55}\mathrm{Mn},A'} - \left(\frac{m(A')-m\left(^{55}\mathrm{Mn}\right)}{m(A')m\left(^{55}\mathrm{Mn}\right)} \right) M}{F}. \tag{5.5}$$

The result of this calculation is presented in Figure 5.7 and Table 5.2.

Table 5.2: *Overview of measured $\delta\langle r^2 \rangle$. The change is calculated relative to ^{55}Mn. The first uncertainty is due to the isotope shift, the second due to the uncertainty on the field and mass shift factors.*

		^{51}Mn	^{53}Mn	^{57}Mn	^{59}Mn	^{61}Mn	^{63}Mn
Exp.	$\delta\langle r^2 \rangle$ [fm^2]	-0.15	-0.27	0.212	0.36	0.552	0.76
	ϵ_{IS} [fm^2]	0.03	0.02	0.009	0.01	0.007	0.02
	$\epsilon_{F,M}$ [fm^2]	0.27	0.10	0.061	0.12	0.170	0.22
Lit. [45]	$\delta\langle r^2 \rangle$ [fm^2]	-0.023	-0.292	-	-	-	-
	ϵ [fm^2]	0.045	0.004	-	-	-	-

Figure 5.7: *The change in mean square charge radius for the different isotopes. The change is calculated based on ^{55}Mn. The dashed lines indicate the uncertainty due to the uncertainty on the field and mass factors.*

Although the scale is quite large, due to the fact that the isotope chain is quite long, no unexpected behavior is seen. The abrupt change in slope is the influence of the $N = 28$ magic number, and a very slight difference in slope can be perceived in the evolution from $N = 28$ to $N = 32$, and from $N = 34$ to $N = 38$.

The focus of this work has been the spin determination and the interpretation of the magnetic moments. The charge radii have been included to form a more complete picture of the region, but their significance has not yet been fully analyzed. Future experiments can focus on a more accurate measurement of the quadrupole moment, combined with an interpretation of the charge radii. This will give a more detailed description of the nuclear structure, including the behavior around $N = 32$.

Chapter 6

Conclusion

A conclusion is simply the place
where you got tired of thinking.

ARTHUR BLOCH OR DAN CHAON

6.1 Summary

Collinear laser spectroscopy was used to measure the hyperfine spectrum of the odd
mass isotopes in the $^{51-63}$Mn chain. The background in these measurements was
suppressed using a bunched beam. From these spectra, the spin, magnetic moment
and the difference in mean square charge radius was extracted. The focus of this
work was on the magnetic moments, which were compared to GXPF1 calculations.

Table 6.1: *New summary of properties for the ground state of Mn isotopes.*

Isotope	N	Spin	Half-life	Magnetic moment $[\mu_\mathbf{n}]$	Ref.
^{51}Mn	26	5/2−	46.2 min.	3.5683(13)	[29, 37]
^{53}Mn	28	7/2−	3.74 megayears	5.035(1)	[29, 38]
^{55}Mn	30	5/2−	-	3.4687179(9)	[29, 39]
^{57}Mn	32	5/2−	85.4 s.	3.486(9)	This work
^{59}Mn	34	5/2−	4.59 s.	3.497(8)	This work
^{61}Mn	36	5/2−	0.67 s.	3.536(8)	This work
^{63}Mn	38	5/2−	0.75 s.	3.44(1)	This work

The physics motivation behind this experiment is the interesting, rapid development of collectivity in this area of the nuclear chart. The spin of several of these isotopes was also not definitively assigned prior to this work.

The final results, as summarized in Table 6.1, allowed for definitive spin assignments and a discussion about the development of collectivity near $N = 40$, specifically the role of the $\nu g_{9/2}$-level.

6.2 Conclusions

The information as provided by the experiment confirmed the tentative assignment of $I = 5/2$ for ^{59,61,63}Mn.

The magnetic moment revealed a contribution of the $g_{9/2}$-level as $N = 40$ is approached. Above $N = 34$, the discrepancy by not including the $g_{9/2}$-level in calculations is noticeable. This means that there is no shell gap at $N = 40$ for $Z = 25$. Interpreting the data under the assumptions of the Nilsson model, a deformation between 0.1 and 0.2 is expected; a smaller deformation would result in deviations from the calculations at a later stage, while a greater one would give earlier deviations.

Measurements of the deformation, available through the quadrupole moment, would be very valuable in the interpretation of the structure of these neutron-rich Mn isotopes. Combined with data on the charge radii, this will allow for a more complete mapping of the evolution of nuclear structure in and around Mn.

Bibliography

[1] **M. De Rydt**. *A dedicated β-NMR/β-NQR setup for LISE-GANIL and study of the nuclear moments of the neutron-rich Al and Cl isotopes.* Ph.D. thesis, KULeuven (2010). URL `https://lirias.kuleuven.be/handle/123456789/256023`.

[2] **K. S. Krane**. *Introductory Nuclear Physics.* John Wiley & Sons (1988).

[3] **P. Van Duppen**. *The deformed Shell Model: Nilsson Model.* In: *Theoretical Nuclear Physics (course)*. KULeuven (2013).

[4] **R. F. Casten**. *Nuclear Structure From A Simple Perspective.* Oxford University Press (1990). ISBN 0-19-504599-8.

[5] **O. Sorlin**. *Shell closure, magic and exotic nuclei* (2009).

[6] **H. Noya, A. Arima, and H. Horie**. *Nuclear Moments and Configuration Mixing.* In: *Supplement of Progress in Theoretical Physics*, , no. 8: pp. 33–112 (1958). URL `http://dx.doi.org/10.1143/PTPS.8.33`.

[7] **T. Otsuka**. *Shell Structure of Exotic Nuclei.* In: *The Euroschool Lectures on Physics with Exotic Beams, Vol. III*, Lecture Notes in Physics, pp. 1–25 (2009). ISBN 978-3-540-85838-6. URL `http://dx.doi.org/10.1007/978-3-540-85839-3`.

[8] **I. Hamamoto and B. Mottelson**. *Shape deformations in atomic nuclei* (2012). URL `http://dx.doi.org/10.4249/scholarpedia.10693`.

[9] **T. Mizusaki**. *Shell model calculation – from basics to the latest methods.*

[10] **E. Caurier, G. Martinez-Pinedo, and F. Nowacki**. *The shell model as a unified view of nuclear structure.* In: *Reviews of Modern Physics*, **volume 77**, no. 2: pp. 427–488 (2005). URL `http://rmp.aps.org/abstract/RMP/v77/i2/p427_1`.

[11] **A. P. Zuker et al.** *Spherical shell model description of rotational motion.* In: *Physical Review C*, **volume 52**, no. 4: pp. 1741–1745 (1995). URL `http://dx.doi.org/10.1103/PhysRevC.52.R1741`.

[12] **M. Honma et al.** *New effective interaction for pf-shell nuclei and its implications for the stability of the N=Z=28 closed core.* In: *Physical Review C*, **volume 69**, no. 3: p. 034335 (2004). ISSN 0556-2813. URL `http://dx.doi.org/10.1103/PhysRevC.69.034335`.

[13] **L. Ballentine**. *Quantum Mechanics: a modern development.* World Scientific Publishing (1998). URL `http://www-dft.ts.infn.it/\protect\T1\textdollar\sim$resta/fismat/ballentine.pdf`.

[14] **J. J. Sakurai and J. Napolitano**. *Modern Quantum Mechanics.* Addison-Wesley, 2e edition (2011).

[15] **D. Griffiths**. *Introduction to electrodynamics.* Pearson Benjamin Cummings, San Francisco (2008). ISBN 0-13-919960-8.

[16] **S. Cottenier and M. Rots**. *Hyperfine Interactions and their Applications in Nuclear Condensed Matter Physics: a microscopic introduction* (2005).

[17] **NIST**. *Physical Reference data* (2013). URL `http://physics.nist.gov/cuu/index.html`.

[18] *Atomic Nucleus.* URL `http://encyclopedia2.thefreedictionary.com/Atomic+Nucleus`.

[19] **K. D. Kreim**. *Collinear Laser Spectroscopy of Potassium.* Ph.D. thesis, Heidelberg (2013).

[20] **P. Magnante and H. Stroke**. *ISOTOPE SHIFT BETWEEN ^{209}Bi AND 6.3-DAY ^{206}Bi.* In: *Journal of the Optical Society of America*, **volume 59**, no. 7: pp. 836–841 (1969). URL `http://www.osti.gov/scitech/biblio/4781263`.

[21] **H. Heylen**. *Spin, magnetic moment and charge radius of 51K.* Master thesis, Katholieke Universiteit Leuven (2012). URL `http://fys.kuleuven.be/iks/nm/files/thesis/hanne-heylen-thesis.pdf`.

[22] **B. Cheal and K. T. Flanagan**. *Progress in laser spectroscopy at radioactive ion beam facilities.* In: *Journal of Physics G: Nuclear and Particle Physics*, **volume 37**, no. 11: p. 113101 (2010). ISSN 0954-3899. URL `http://dx.doi.org/10.1088/0954-3899/37/11/113101`.

[23] **University of Mainz**. *TRIGA-Laser*. URL `http://www.uni-mainz.de/FB/Chemie/AK-Noertershaeuser/en/experiments/triga-laser/`.

[24] **M. Wang et al.** *The AME 2012 atomic mass evaluation*. In: *Chinese Physics C*, **volume 36**, no. 12: pp. 1603–2014 (2012).

[25] **J. Wang**. *Dicke narrowing and speed-dependent effects in dispersion signals*. Ph.D. thesis, UmeåUniversity, Sweden (2013).

[26] *ISOLDE Layout* (2008). URL `http://isolde.web.cern.ch/sites/isolde.web.cern.ch/files/ISOLDE_layout.pptx`.

[27] **N. Hoteling et al.** *Rotation-aligned coupling in Fe61*. In: *Physical Review C*, **volume 77**, no. 4: p. 044314 (2008). ISSN 0556-2813. URL `http://dx.doi.org/10.1103/PhysRevC.77.044314`.

[28] **D. Steppenbeck et al.** *Magnetic rotation and quasicollective structures in ^{58}Fe: Influence of the $\nu g_{9/2}$ orbital*. In: *Physical Review C*, **volume 85**, no. 4: p. 044316 (2012). ISSN 0556-2813. URL `http://dx.doi.org/10.1103/PhysRevC.85.044316`.

[29] **Brookhaven National Laboratory**. *National Nuclear database*. URL `http://www.nndc.bnl.gov/`.

[30] **National Nuclear Data Center**. *Evaluated Nuclear Structure Data File* (2014). URL `http://www.nndc.bnl.gov/ensdf/`.

[31] **B. Cheal et al.** *Nuclear Spins and Moments of Ga Isotopes Reveal Sudden Structural Changes between N=40 and N=50*. In: *Physical Review Letters*, **volume 104**, no. 25: p. 252502 (2010). ISSN 0031-9007. URL `http://dx.doi.org/10.1103/PhysRevLett.104.252502`.

[32] **T. Baugher et al.** *Intermediate-energy Coulomb excitation of $^{58,60,62}Cr$: The onset of collectivity toward N=40*. In: *Physical Review C*, **volume 86**, no. 1: p. 011305 (2012). ISSN 0556-2813. URL `http://dx.doi.org/10.1103/PhysRevC.86.011305`.

[33] **B. Cheal et al.** *Collinear laser spectroscopy of manganese isotopes using optical pumping in ISCOOL*. Research proposal.

[34] **K. Kaneko et al.** *Shell model study of single-particle and collective structure in neutron-rich Cr isotopes*. In: *Physical Review C*, **volume 78**, no. 6: p. 064312 (2008). ISSN 0556-2813. URL `http://dx.doi.org/10.1103/PhysRevC.78.064312`.

[35] **C. Guénaut et al.** *High-precision mass measurements of nickel, copper, and gallium isotopes and the purported shell closure at N=40.* In: *Physical Review C*, **volume 75**, no. 4: p. 044303 (2007). ISSN 0556-2813. URL `http://dx.doi.org/10.1103/PhysRevC.75.044303`.

[36] **B. Cheal et al.** *Laser Spectroscopy of Niobium Fission Fragments: First Use of Optical Pumping in an Ion Beam Cooler Buncher.* In: *Physical Review Letters*, **volume 102**, no. 22: p. 222501 (2009). ISSN 0031-9007. URL `http://dx.doi.org/10.1103/PhysRevLett.102.222501`.

[37] **J. Jönsson et al.** *Hyperfine structure investigations of ^{51}Mn and ^{52m}Mn.* In: *Nuclear Physics A*, **volume 66**: pp. 306–316 (1971). URL `http://www.sciencedirect.com/science/article/pii/0375947471904337`.

[38] **W. Dobrowolski, R. Jones, and C. Jeffries**. *Spin and Magnetic Moment of Mn^{53}.* In: *Physical Review*, **volume 104**, no. 1952: pp. 1950–1952 (1956). URL `http://prola.aps.org/abstract/PR/v104/i5/p1378_1`.

[39] **O. Lutz and W. Steinkilberg**. *^{55}Mn NMR Studies in Aqueous Permanganate Solutions.* In: *Zeitschrift für Naturforschung*, **volume 29a**: pp. 1467–1470 (1974).

[40] **J. Beringer et al.** *Review of Particle Physics.* In: *Physical Review D*, **volume 86**, no. 1: p. 010001 (2012). ISSN 1550-7998. URL `http://dx.doi.org/10.1103/PhysRevD.86.010001`.

[41] **NIST**. *Weighted standard deviation* (1996). URL `http://www.itl.nist.gov/div898/software/dataplot/refman2/ch2/weightsd.pdf`.

[42] **W. I. F. David**. *Powder diffraction peak shapes. Parameterization of the pseudo-Voigt as a Voigt function.* In: *Journal of Applied Crystallography*, **volume 19**: pp. 63–64 (1986).

[43] **H. Di Rocco and A. Cruzado**. *The Voigt Profile as a Sum of a Gaussian and a Lorentzian Functions, when the Weight Coeffcient Depends Only on the Widths Ratio.* In: *Acta Physica Polonica A*, **volume 122**, no. 4: pp. 666–669 (2012).

[44] **N. Stone**. *Table of nuclear magnetic dipole and electric quadrupole moments.* In: *Atomic Data and Nuclear Data Tables*, **volume 90**, no. 1: pp. 75–176 (2005). ISSN 0092640X. URL `http://dx.doi.org/10.1016/j.adt.2005.04.001`.

[45] **F. Charlwood et al.** *Ground state properties of manganese isotopes across the shell closure.* In: *Physics Letters B*, **volume 690**, no. 4: pp. 346–351

(2010). ISSN 03702693. URL `http://dx.doi.org/10.1016/j.physletb.2010.05.060`.

[46] **J. Papuga**. *Shell-model calculations for Co and Mn isotopes*. Technical report, KU Leuven, Leuven (2013).

[47] **Y. Sun et al.** *Projected shell model study for neutron-rich, odd-odd Mn isotopes*. In: *Physical Review C*, **volume 85**, no. 5: p. 054307 (2012). ISSN 0556-2813. URL `http://dx.doi.org/10.1103/PhysRevC.85.054307`.

[48] **P. Moller et al.** *Nuclear ground-state masses and deformations*. In: *At. Data Nucl. Data Tables*, **volume 59**, no. 2: pp. 185–381 (1995). URL `http://dx.doi.org/10.1006/adnd.1995.1002`.

[49] **W. H. King**. *Isotope Shifts in Atomic Spectra*. Plenum Press, New York (1984). ISBN 0-306-41562-3.

[50] **B. Cheal**. *Status of the Mn analysis*. In: *Mn meeting*. Leuven (2013).

FACULTEIT WETENSCHAPPEN
DEPARTEMENT NATUURKUNDE EN STERRENKUNDE
NUCLEAR MOMENTS GROUP
Celestijnenlaan 200D bus 2402
B-3001 Heverlee
wouter.gins@student.kuleuven.be
http://fys.kuleuven.be/iks/nm/home